α-Actinin and fimbrin cooperate with myosin II to organize actomyosin bundles during contractile-ring assembly

Damien Laporte[a], Nikola Ojkic[b], Dimitrios Vavylonis[b], and Jian-Qiu Wu[a,c]
Departments of [a]Molecular Genetics and [c]Molecular and Cellular Biochemistry, The Ohio State University, Columbus, OH 43210; [b]Department of Physics, Lehigh University, Bethlehem, PA 18015

ABSTRACT The actomyosin contractile ring assembles through the condensation of a broad band of nodes that forms at the cell equator in fission yeast cytokinesis. The condensation process depends on actin filaments that interconnect nodes. By mutating or titrating actin cross-linkers α-actinin Ain1 and fimbrin Fim1 in live cells, we reveal that both proteins are involved in node condensation. Ain1 and Fim1 stabilize the actin cytoskeleton and modulate node movement, which prevents nodes and linear structures from aggregating into clumps and allows normal ring formation. Our computer simulations modeling actin filaments as semiflexible polymers reproduce the experimental observations and provide a model of how actin cross-linkers work with other proteins to regulate actin-filament orientations inside actin bundles and organize the actin network. As predicted by the simulations, doubling myosin II Myo2 level rescues the node condensation defects caused by Ain1 overexpression. Taken together, our work supports a cooperative process of ring self-organization driven by the interaction between actin filaments and myosin II, which is progressively stabilized by the cross-linking proteins.

INTRODUCTION

Actin filaments, myosin motors, actin cross-linkers, and other proteins self-organize into contractile structures of various morphologies. Fungi and animal cells dramatically reorganize their actin cytoskeleton to form the contractile ring that partitions a mother cell into two daughter cells during cytokinesis (Balasubramanian et al., 2004; Barr and Gruneberg, 2007; Pollard and Wu, 2010; Laporte et al., 2010). This global restructuring is achieved by a combination of actin filament assembly through de novo polymerization (Pelham and Chang, 2002; Wu et al., 2006; Watanabe et al., 2008; Zhou and

Wang, 2008; Coffman et al., 2009), disassembly by severing (Nakano and Mabuchi, 2006; Chen and Pollard, 2011), cross-linking/bundling (Guha et al., 2005; Murthy and Wadsworth, 2005; Medeiros et al., 2006; Nakano and Mabuchi, 2006; Reichl et al., 2008), and/or cortical flow (Noguchi et al., 2001; Zhou and Wang, 2008). Previous in vitro studies have shown that passive actin filament cross-linking controls the mechanical and dynamic properties of active actin gels (Bendix et al., 2008; Banerjee et al., 2011; Kohler et al., 2011). We took advantage of the simplicity of genetic engineering of fission yeast *Schizosaccharomyces pombe* to study the role of actin cross-linking quantitatively during contractile-ring formation in live cells. Combining experiments and theoretical modeling we showed that the morphology of the contractile ring can be modulated by controlled changes in the concentrations of the two main fission yeast passive actin filament cross-linkers, α-actinin and fimbrin.

α-Actinins and fimbrins are actin bundling/cross-linking proteins with their biochemical properties characterized in vitro (Xu et al., 1998; Bartles, 2000; Nakano et al., 2001; Skau and Kovar, 2010; Skau et al., 2011), and some crystal structures have been solved (Klein et al., 2004; Sjoblom et al., 2008). Fimbrin monomers bundle actin filaments into tight bundles with two adjacent actin-binding domains (ABD). α-Actinin cross-links actin filaments into a network by forming an antiparallel homodimer having one ABD on each

polypeptide separated by spectrin-like repeats. α-Actinins reduce disruption of the actin network in the presence of a severing factor and high-rate deformation in vitro (Sato *et al.*, 1987; Maciver *et al.*, 1991; Schmoller *et al.*, 2011) and regulate the movements of single actin filaments through myosin II (Janson *et al.*, 1992). However, molecular mechanisms of their in vivo functions remain poorly understood.

In fission yeast, the actin filaments of the contractile ring are mainly assembled de novo by formin Cdc12 at the division site (Chang *et al.*, 1997; Pelham and Chang, 2002; Kovar *et al.*, 2003; Coffman *et al.*, 2009). Two sequential pathways are critical for the efficient assembly of a functional contractile ring at the cell equator. The first relies on cytokinesis nodes that assemble in an equatorial broad band and subsequently condense into a compact ring (Bähler *et al.*, 1998a; Motegi *et al.*, 2000; Wu *et al.*, 2003, 2006; Vavylonis *et al.*, 2008; Laporte *et al.*, 2011; Padmanabhan *et al.*, 2011). The nodes contain anillin-like Mid1, IQGAP Rng2, myosin II, F-BAR protein Cdc15, and formin Cdc12. In the Search, Capture, Pull, and Release (SCPR) model (Vavylonis *et al.*, 2008), Cdc12 nucleates actin filaments that grow out of nodes, and myosin II pulls on these filaments and condenses the nodes into a ring by establishing transient actomyosin connections among nodes. To account for the transient linear structures observed during ring formation, a theoretical node alignment mechanism, consisting of short-range aligning forces, has been proposed (Ojkic *et al.*, 2011). The second pathway for ring formation depends on the septation-initiation network (SIN), which also matures the compact ring and triggers its constriction (Wachtler *et al.*, 2006; Hachet and Simanis, 2008; Roberts-Galbraith and Gould, 2008).

In *S. pombe*, α-actinin Ain1 and fimbrin Fim1 localize to the division site and have overlapping functions in cytokinesis (Nakano *et al.*, 2001; Wu *et al.*, 2001; Skau and Kovar, 2010). Genetic, deletion, and overexpression data indicate that Ain1 and Fim1 participate in contractile-ring formation (Nakano *et al.*, 2001; Wu *et al.*, 2001). Actin filaments arrest as a meshwork of aberrant filaments/bundles at the equator in some *ain1* and *fim1* mutants (Nakano *et al.*, 2001; Wu *et al.*, 2001; Skau *et al.*, 2011). However, their precise roles in cytokinesis remained elusive. By changing their concentrations, we found that Ain1 and Fim1 are essential for node condensation into the contractile ring. They stabilize linear actomyosin structures that form during late stages of node condensation and thus provide a mechanism for the proposed node alignment (Ojkic *et al.*, 2011). We developed a computational model of how the observed actin network structures depend on the concentrations of actin cross-linkers and myosin motors. Collectively our work indicates that α-actinin and fimbrin are critical for contractile-ring assembly by stabilizing linear actomyosin structures.

RESULTS
In this study, we define the beginning of node condensation (when nodes begin to move toward each other) as time 0 and used it to align all the measurements except where noted. We define nodes as discrete protein clusters (20–65 discernible puncta) at the equatorial plasma membrane; linear structures as thin and elongated structures surrounded by nodes; and clumps as bright rounder structures without surrounding nodes nearby.

Normal node condensation depends on α-actinin Ain1 and fimbrin Fim1
We hypothesized that actin cross-linkers α-actinin Ain1 and fimbrin Fim1 contribute to the local node alignment suggested theoretically (Ojkic *et al.*, 2011). To test this idea, we deleted *ain1* and *fim1* and

observed ring formation using myosin II light chain Rlc1 or heavy chain Myo2 as node markers. In wild-type (wt) cells, a broad band of nodes condensed into a more or less uniform ring 11.7 ± 1.8 min after the start of node condensation (n = 26 cells; Figure 1A, top left; Video 1; Supplemental Figure S1, A and B). In *fim1Δ*, the ring formed normally (12.1 ± 2.3 min; n = 11; Figure 1A, top right), consistent with previous reports (Nakano *et al.*, 2001; Wu *et al.*, 2001). In contrast, the formation of a uniform ring was delayed in 52% of *ain1Δ* cells (26.2 ± 12.3 min; n = 77), in which nodes condensed into 1–3 clumps that took 10–30 additional min to rearrange into a uniform ring (Figure 1A, bottom left; Video 1). By imaging Mid1-mECitrine, the anillin-like node scaffolding protein, we confirmed that the defect in *ain1Δ* occurred during node condensation but not during node formation (Supplemental Figure S1C). Next we investigated node condensation in the absence of both cross-linkers. Because *ain1Δ fim1Δ* is synthetic lethal (Wu *et al.*, 2001), we mimicked the double deletion by combining *ain1Δ* with *fim1* expressed from a medium-strength *41nmt1* promoter. Under the repressing condition, ring formation was severely affected (54.5 ± 10.4 min; n = 36), where 100% of the cells condensed Myo2 nodes into clumps (Figure 1A, bottom right; Video 2). The same abnormal condensation was observed in *ain1Δ fim1Δ* cells from germinated spores (Supplemental Figure S1D). Node formation and initial distribution were normal in the mutants just mentioned (Supplemental Figure S1, A and B). Thus both Ain1 and Fim1 are involved in proper node condensation.

To clarify the functional relationship between Fim1 and Ain1 during node condensation, we first investigated the timing of their localization to the cell equator. In wt cells, we found that Ain1 appeared at the cell equator with ~20 molecules when nodes started to condense and gradually increased to ~390 molecules at the end of condensation (Figure 1C; Supplemental Figure S1, E and F). Fim1 appeared later at the cell equator, near the end of node condensation (Supplemental Figure S1, E and G). We found that Ain1 and Fim1 do not affect each other's timing and pattern of localization (Supplemental Figure S1, E–G). Because Fim1 depletion/deletion increases the clumping phenotype in *ain1Δ* (see preceding paragraph), we tested whether Fim1 overexpression can rescue abnormal node condensation in *ain1Δ*. Interestingly, when we overexpressed Fim1 (~9 times compared to wt; Supplemental Figure S1H) in *ain1Δ* cells, 100% of the cells condensed monomeric enhanced green fluorescent protein (mEGFP)-Myo2 nodes normally into the contractile ring (n = 19; Figure 1B). These data indicate that fimbrin and α-actinin function in an orderly manner, whereas Fim1 acts subsidiarily to Ain1 during node condensation.

α-Actinin Ain1 has an overlapping function with the SIN pathway in contractile-ring formation
The SIN pathway is required for the formation of a homogeneous contractile ring, involving at least one node protein, the F-BAR protein Cdc15 (Wachtler *et al.*, 2006; Hachet and Simanis, 2008). Given the clump and abnormal ring formation in *ain1Δ*, we investigated the relationship among the SIN pathway, Cdc15, and Ain1. The formation of a contractile ring from the clumps in *ain1Δ* depended on the SIN pathway as a compact ring was formed in *ain1Δ* and SIN single mutants but not in the double mutants (Supplemental Figure S2A). Moreover, *ain1Δ* was synthetic lethal/sick with SIN mutants *cdc7-24* and *cdc11-123*, and with *cdc15-140* at semirestrictive temperatures (Supplemental Figure S2B), which suggests they function in separate genetic pathways and so may not affect each other's localizations. Indeed, Ain1 localized normally in the ring with Rlc1 in SIN and *cdc15-140* mutants at 36°C (n ≥ 15 cells;
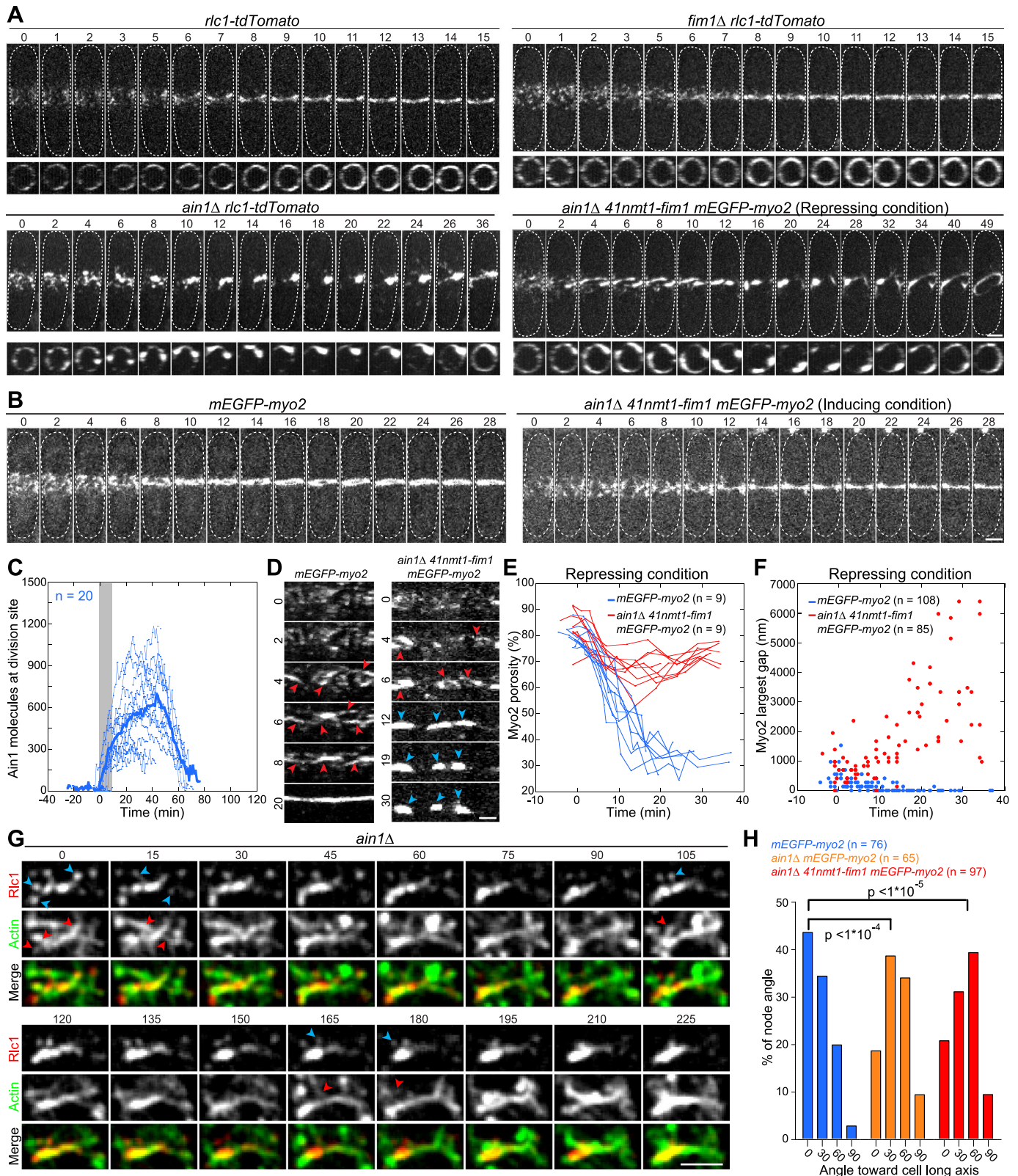
FIGURE 1: Normal node condensation during contractile-ring assembly depends on α-actinin Ain1 and fimbrin Fim1. Start of node condensation is defined as time 0. Cells were grown in YE5S + thiamine at 5 µg/ml (repressing condition for *nmt1* promoters) for 22 h except in B, C, and G. (A) Deletion (or depletion) of *ain1* and/or *fim1* induces clump formation during node condensation. Elapsed times are in minutes. Time courses of node condensation in wt, *fim1Δ*, *ain1Δ*, and *ain1Δ 41nmt1-fim1* cells are shown. Also see Videos 1 and 2. For each strain, top panels are maximum intensity projections; bottom panels are 90° rotations. The complete ring is defined as a continuous line without any surrounding signal at cell equator on maximum intensity projections. (B) Moderate Fim1 overexpression can rescue

Supplemental Figure S2, C and D). Moreover, neither Cdc15 localization nor its concentration was affected in ain1Δ (Supplemental Figure S2, E and F). Thus Ain1 and the SIN pathway play overlapping roles in contractile-ring assembly.

Unstable linear structures strongly bias the direction of node movement

To elucidate the roles of Ain1 and Fim1 in ring formation, we quantified node condensation. During the late stages of node condensation in wt cells, Myo2 and Rlc1 formed transient linear structures that preceded a compact ring (Figure 1D, red arrowheads). Without enough actin cross-linkers (in ain1Δ 41nmt1-fim1 or ain1Δ), linear structures and surrounding nodes collapsed into clumps (Figure 1D; Supplemental Figure S1I, blue arrowheads). Given that Ain1 and Fim1 localize to the cell equator during node condensation (Figure 1C; Supplemental Figure S1E), these data suggest that both actin cross-linkers may act on the linear structures formed during the late stages of node condensation.

The SCPR model predicts that the lack of stabilization of the linear structures leads to large gaps (defined as the length of circumferential gaps in node signal; see *Materials and Methods*) and increased porosity (a measure of the fraction of space between nodes; Ojkic *et al.*, 2011). In ain1Δ 41nmt1-fim1 and ain1Δ cells, both the porosity (Figure 1E; Supplemental Figure S1J) and the largest gap (Figure 1F; Supplemental Figure S1K) between nodes were bigger during node condensation compared with those in wt. These experiments suggest that both Ain1 and Fim1 stabilize linear structures. To understand how unstable linear structures lead to clump formation, we simultaneously observed actin filaments and nodes. In ain1Δ, after a linear structure formed, most surrounding nodes became connected by actin filaments/bundles marked with GFP-CHD (calponin homology domain from IQGAP Rng2; Wachtler *et al.*, 2003; Martin and Chang, 2006) and pulled to the linear structure to form a clump (Figure 1G; Video 3). We measured the angles of node displacements with respect to the cell's long axis. In wt, 78% of the nodes moved toward the cell center with an angle between 0° and 30°. However, only 58% and 52% of nodes displayed this orientation in ain1Δ or ain1Δ 41nmt1-fim1, respectively (Figure 1H). These abnormal orientations rendered inhomogeneities in node location, which are predicted to result in clump formation (Vavylonis *et al.*, 2008; Ojkic and Vavylonis, 2010; Ojkic *et al.*, 2011). Together actin cross-linkers may stabilize linear structures by preventing their aggregation of nearby nodes during the late stages of node condensation.

Ain1 overexpression promotes stable linear structure formation

As the transient linear structures appear to be unstable without Ain1, we reasoned that Ain1 overexpression has the opposite effect.

Ain1 concentrations were modulated using *nmt1* promoters with different strengths (*3nmt1* is the strongest, and *81nmt1* is the weakest). Global α-actinin concentrations were increased to 3–18 times the wt Ain1 level (Figure 2A, top graph; Supplemental Figure S3, A and B). At the division site, the Ain1 levels increased to 4, 8, and 15 times the wt level, respectively (Figure 2A, bottom graph). Interestingly, Ain1 concentration had no obvious effect on its dynamics in FRAP assays ($t_{1/2}$ = ~20–26 s, p > 0.05 for each compared with wt; Supplemental Figure S3C), indicating that Ain1 dissociates from the contractile ring at a concentration-independent rate.

Next we analyzed the effect of Ain1 and Fim1 concentrations on node distribution and condensation. Neither Ain1 nor Fim1 levels had significant effects on initial node distribution before condensation (Supplemental Figures S3, D and E, and S4B). Surprisingly, node condensation was dramatically affected as a function of Ain1 overexpression (Figure 2B; Video 4). Nodes condensed into numerous linear structures (Figure 2C). These structures slowly organized into tilted or double rings over time (Figure 2B; Video 4). Unlike the compensation of ain1Δ deletion by the moderate Fim1 overexpression (Figure 1B), strong Fim1 overexpression led to highly elongated cells with severe cytokinesis defects (Supplemental Figure S4A). When Fim1 was highly overexpressed in otherwise wt cells, nodes did not condense but spread along the long axis of the cell instead and thus delayed cytokinesis (Supplemental Figure S4B; Video 5). During this process, some Rlc1 linear structures were observed but rapidly disappeared after their formation (Supplemental Figure S4C), and faint actin filaments/bundles were detectable using GFP-CHD (Supplemental Figure S4D). Together these results suggest that actin cross-linkers affect node condensation through linear structure formation/stabilization (see *Discussion*).

Actin cross-linkers regulate actin cytoskeleton dynamics and node movement

During node condensation, Ain1 localized to the equator between nodes and sometimes overlapped with them (Figure 3, A and B). Ain1 also colocalized with actin filaments at the division site (Figure 3C). Given that α-actinin family proteins are known actin cross-linkers (Xu *et al.*, 1998; Bartles, 2000), we hypothesized that Ain1 regulates node condensation by modifying actin distribution and dynamics. In most anaphase *3nmt1-ain1* cells, GFP-CHD–labeled actin filaments coalesced slowly into disorganized actin structures instead of a contractile ring, with several thick and stable bundles (Figure 3, D and E; Video 6). In addition, the main actin bundles were more stable compared with a wt ring revealed by treating cells with 10 μM latrunculin A (Lat-A), an actin monomer sequestering agent (Figure 3F). The $t_{1/2}$ of decay for GFP-CHD was 5.8 ± 2.3 min in *3nmt1-ain1* cells, 2.5-fold slower than that in wt ($t_{1/2}$ = 2.3 ± 0.8 min; Figure 3G). By contrast, ain1Δ cells were more sensitive to Lat-A treatment than

clump formation induced by ain1Δ. Time courses of node condensation in wt and ain1Δ 41nmt1-fim1 cells increase in the inducing condition in EMM5S liquid medium for 42 h. (C) mEGFP-Ain1 concentrates at the cell equator during node condensation and ring maturation. Timing was determined using Rlc1-tdTomato, and the gray rectangle marks the duration of node condensation. The bold blue line is the mean of individual measurements (thin blue lines). (D) Radial projections of mEGFP-Myo2 forming linear structures (red arrowheads) and clumps (blue arrowheads) during node condensation. (E and F) Two-dimensional porosity and largest gap (see *Materials and Methods*) visualized by mEGFP-Myo2 during node condensation into the contractile ring. (G) Clumps connect with nearby nodes by actin filaments in ain1Δ rlc1-tdTomato 41nmt1-GFP-CHD strain grown in EMM5S for 20 h (also see Video 3). Red arrowheads point to GFP-CHD marked actin filaments linking individual nodes (blue arrowheads) that move toward the clump. Times, in seconds, are relative to the first frame. (H) Node displacements are biased when actin cross-linker levels are reduced. Angles between directions of node displacements and the long cell axis observed during ~3 min. Bars, 2 μm.
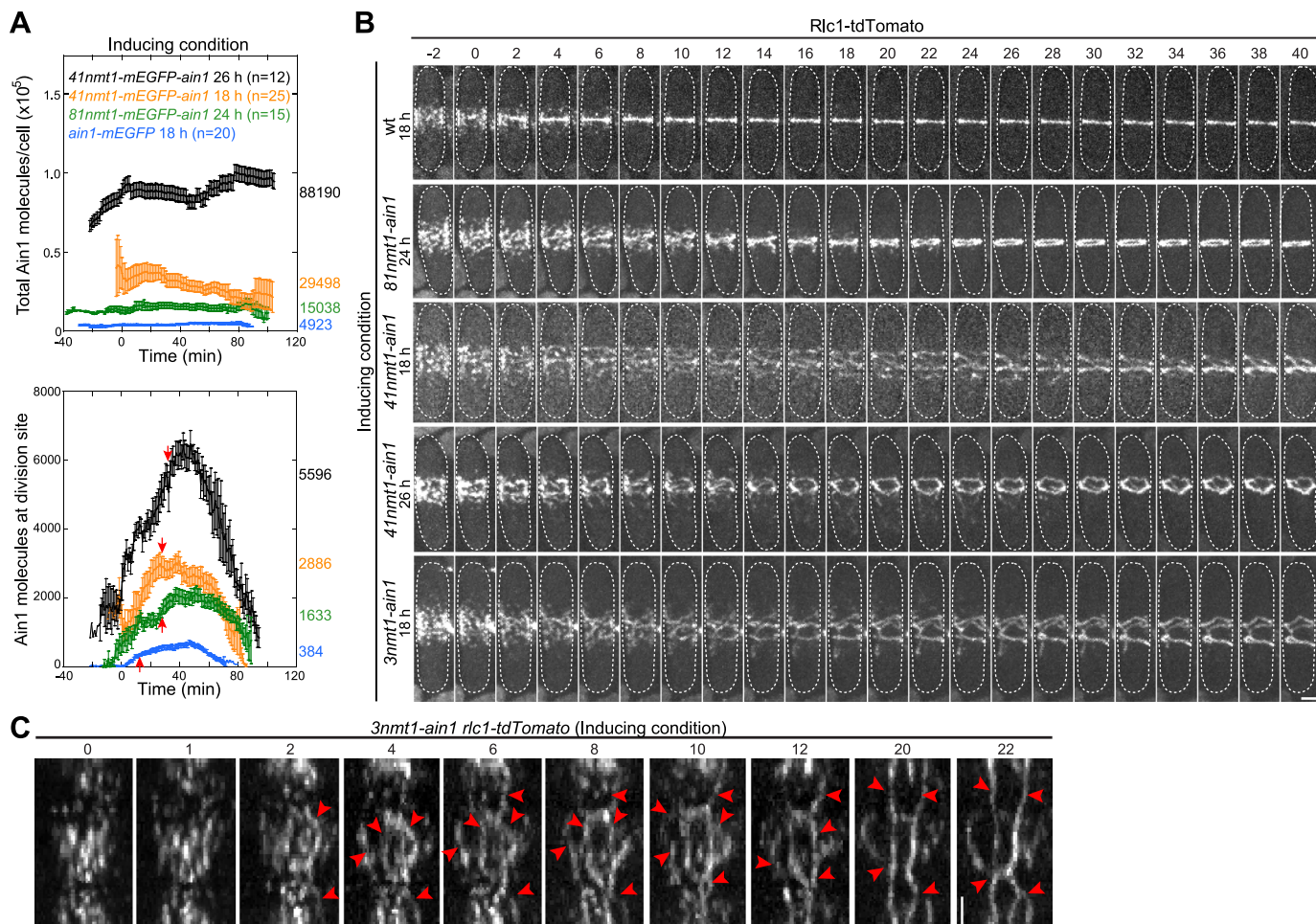
FIGURE 2: Ain1 overexpression promotes the formation of stable linear structures during contractile-ring formation. (A) Ain1 global and local abundance (mean ± SEM) increases with the strength of *nmt1* promoters. Top panel shows total Ain1 molecules in each mitotic cell. Colored numbers on the right of the graph indicate the mean Ain1 molecules over time. Bottom panel shows Ain1 molecules at the division site. Colored numbers are the Ain1 molecules at the end of node condensation, indicated by red arrows. Inducing time in EMM5S is indicated. (B) Ain1 overexpression affects node condensation into the contractile ring. Strains expressing both Rlc1-tdTomato and mEGFP-Ain1 (under different *nmt1* promoters) were imaged. Inducing time in EMM5S is indicated. Elapsed times are in minutes. Also see Video 4. (C) Nodes condense into numerous linear structures when Ain1 is overexpressed. Time course (in minutes) of Rlc1-tdTomato radial projections. Red arrowheads indicate representative linear structures. Cells were induced for 18 h in EMM5S. Bars, 2 μm.

were wt cells (Figure 3, F and G). The decay rate of GFP-CHD fluorescence intensity in the contractile ring was approximately twice faster than that in wt (1.0 ± 0.3 min in *ain1Δ*). Phalloidin staining revealed a similar quantity of actin filaments on the cell cortex or in the ring in the different genetic backgrounds (Supplemental Figure S5). Thus Ain1 concentration affects the kinetics of actin filament turnover, but the total actin polymer levels remain approximately constant.

Given that node movements depend on actin filaments, we investigated node behavior during condensation in different crosslinker mutants. First, we investigated the overall node condensation rate by measuring the width of the broad band over time. In wt, Rlc1 nodes condensed at 195 nm/min. The condensation rate decreased with increasing Ain1 concentration, down to 42 nm/min in the strain with the highest overexpression (Figure 4A). Consistently, most nodes had shorter displacements (Figure 4B) when Ain1 was highly overexpressed compared with wt. By contrast, nodes traveled a longer distance over the same period of time in *ain1Δ 41nmt1-fim1*

cells under repressing conditions (Figure 4C). Strong Ain1 overexpression led to a reduction of the frequency of detectable node movement (Figure 4D) and their instantaneous speeds (p < 0.05; Figure 4E). By contrast, these parameters increased in *ain1Δ 41nmt1-fim1* cells (Figure 4, D and F; *p* < 0.05). Collectively these results suggest that cross-linkers stabilize the actin cytoskeleton, restrict node movement during node condensation, and thus help stabilize transient linear structures.

Numerical model of how cross-linking activity controls the morphology of node aggregates

We assume that the biological system is robust enough to allow an approximate description with a model that includes the most important mechanisms revealed by experiments such as actin polymerization, myosin pulling, and cross-linking. To investigate how actin filament cross-linking may contribute to node alignment into linear structures and ring organization, we revised the SCPR model (Vavylonis *et al.*, 2008) to include cross-linking among actin
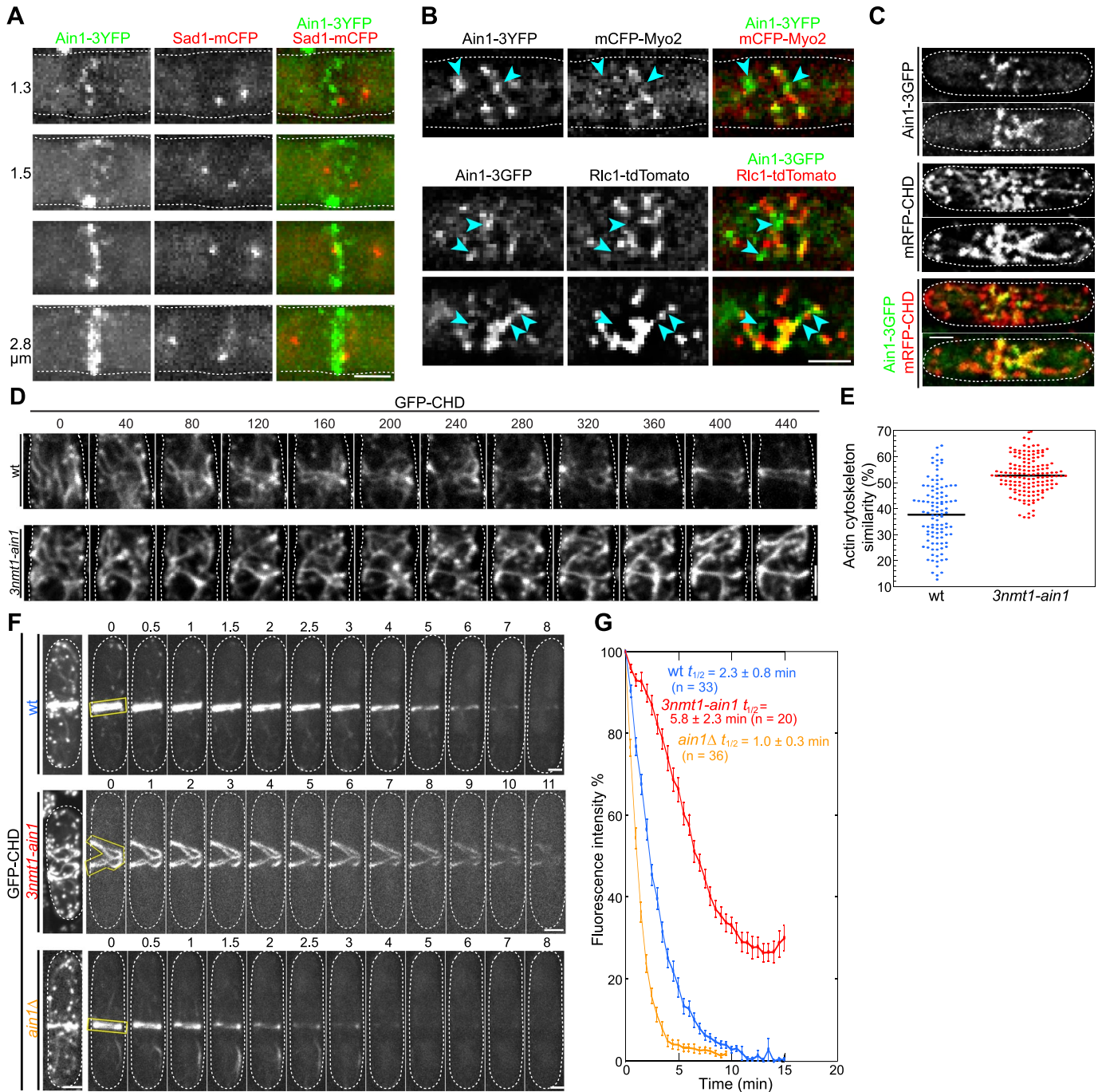
FIGURE 3: Ain1 localizes to the cell-division site during node condensation and regulates actin dynamics. (A) Ain1 localizes to the division site shortly after spindle pole body (SPB) separation. SPBs are marked with Sad1, and the distance between two SPBs is indicated. (B) Ain1 localizes with and between (blue arrowheads) nodes or to linear structures during node condensation. (C) Ain1 colocalizes with actin filaments marked with CHD at cell division site. The *ain1-3GFP 41nmt1-mRFP-CHD* strain was grown in EMM5S for 20 h. Images in B and C are maximum-intensity projections of three planes after deconvolution. (D and E) Actin network coalesces slowly into a few main bundles when Ain1 is overexpressed. Cells were grown in inducing condition for 18 h. (D) Sum projection of two consecutive images with a 10-s delay. Times, in seconds, are relative. Also see Video 6. (E) Quantification of actin cytoskeleton similarity over time (see *Materials and Methods*). The percentages of similarity of GFP-CHD images during ring formation in wt and *3nmt1-ain1* are shown. Bars indicate means. (F and G) Dynamics of the actin ring/network at the division site depends on Ain1 concentrations. WT, *3nmt1-ain1*, and *ain1Δ* cells expressing *41nmt1-GFP-CHD* were grown for 22 h in inducing condition, preincubated with 100 μM Arp2/3 inhibitor for 5 min, then treated with 10 μM Lat-A and imaged immediately at time 0. (F) The cells before time 0 are untreated with either inhibitor. Times are in minutes. (G) Fluorescence decay curves of GFP-CHD after Lat-A treatment with half time (mean ± SD) and cells analyzed indicated. Fluorescence intensity of GFP-CHD ring within yellow polygon as depicted in F was measured. Bars, 2 μm.
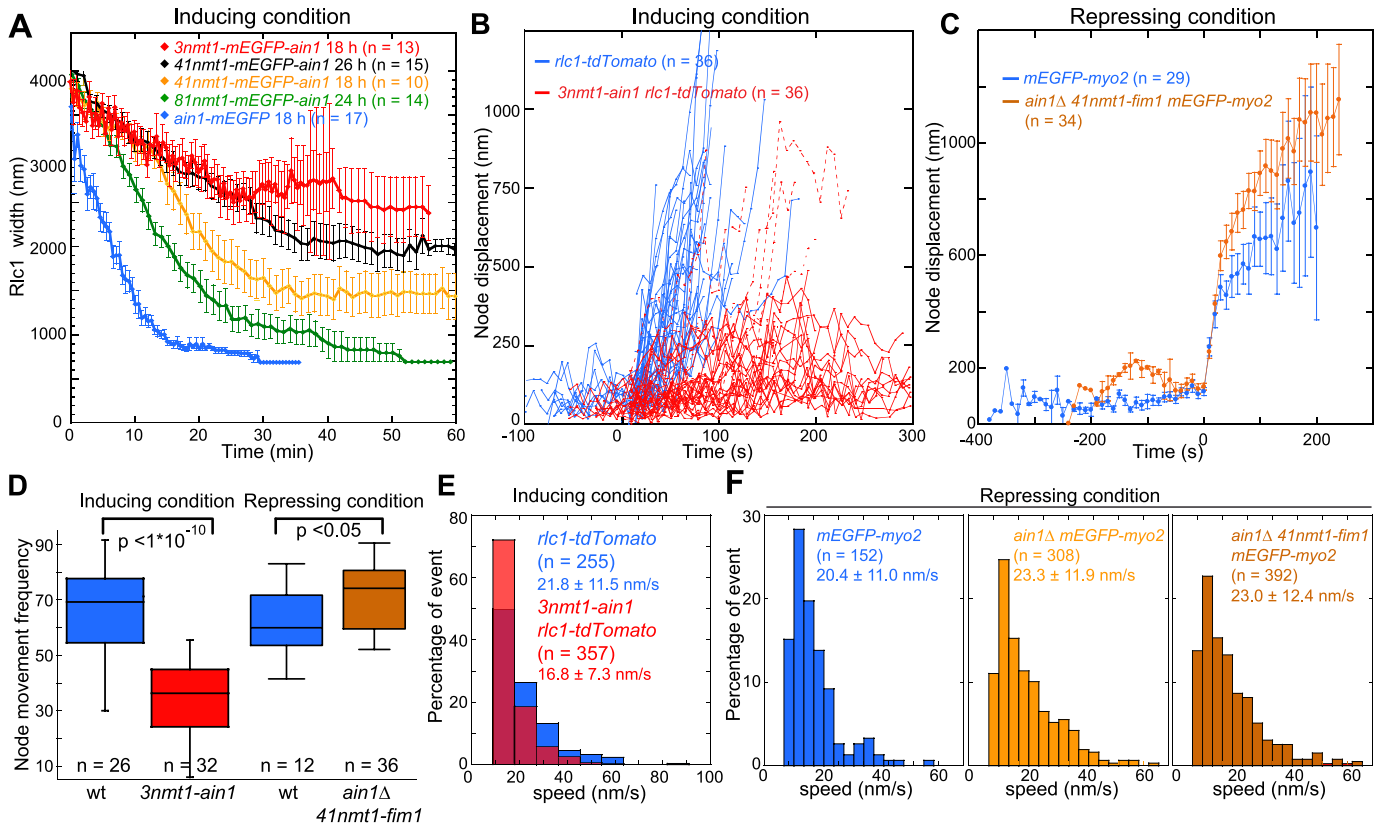
FIGURE 4: Ain1 regulates node movements. (A) Global node condensation rates have an inverse relationship with Ain1 concentrations. Width of Rlc1 broad band (mean ± SEM) was measured over time. Strains, inducing times in EMM5S, and numbers of cells analyzed are depicted. (B, D, and E) Both wt and *3nmt1-ain1* cells were imaged after 18 h in EMM5S. (B) Ain1 overexpression affects individual node displacements. Nodes were tracked over time with a delay of 7 s in wt (blue lines) and *3nmt1-ain1* (red lines). Each line represents an individual node's movement. Red dashed lines are individual displacements >500 nm (6 of 36 total measurements) for *3nmt1-ain1*. (C) Nodes travel a longer distance (mean ± SEM) in *ain1Δ 41nmt1-fim1* cells (delay is 10 s between time points). Cells were grown in YE5S for 22 h. (D) The movement frequency (see *Materials and Methods*) of Rlc1-tdTomato nodes has an inverse relationship with Ain1 concentrations. (E) Instantaneous node speed is reduced when Ain1 is highly overexpressed. Rlc1-tdTomato node movements were tracked every 10 s after the beginning of node condensation. The distributions were superimposed. Note that nodes in *3nmt1-ain1* strains (red) display a slower speed than those in wt (blue). (F) Instantaneous node speeds increase when the levels of actin cross-linkers are reduced. mEGFP-Myo2 node movements in different strains were tracked every 10 s after the beginning of node condensation.

filaments (Figure 5, A–F; Supplemental Figure S6A; see *Materials and Methods*).

In the simulations, formins in each node are assumed to nucleate two actin filaments that grow along random directions on a two-dimensional plane representing the cell's cortex. When the polymerizing filament encounters a neighboring node, the filament is captured and a contractile myosin pulling force is exerted toward the barbed end associated with formins on the nucleating node (Figure 5, A and B). Actin filaments turn over due to filament severing. In the new model, we further allow actin filaments to bend by simulating them as semiflexible polymers consisting of beads connected by springs (Nedelec and Foethke, 2007). In our coarse-grained description we represent cross-linking by an attractive interaction between filament beads (Figure 5C). The rate of cross-linking was tuned by adjusting the range of this interaction potential, described by parameter α (equal to the ratio of the range of the interaction potential divided by the distance between the beads). Small (large) values of α correspond to slow (fast) cross-linking rates between filaments. The magnitude of the cross-linker dissociation rate depends on

both α and the depth of the interaction potential, proportional to parameter k_{cross}. We assume k_{cross} is sufficiently small to allow anti-parallel bundles to form by filaments that grow toward one another while remaining aligned (Figure 5, E and F). Strong cross-linking of growing filaments (large k_{cross}) results in filament buckling and alignment into parallel cable-like bundles (Figure 5F). Most actin cross-linkers bind to actin filaments transiently in vitro (Xu *et al.*, 1998; Strehle *et al.*, 2011), consistent with our assumption of small enough k_{cross}. We limit the magnitude of pulling forces when nodes connect with bundles of filaments to account for the myosin force being distributed over many filaments and for the interference of myosin activity with actin cross-linkers (Figure 5D). Unlike Ojkic *et al.* (2011), we do not impose node alignment by forces other than those that arise from cross-linkers.

Simulations reproduced the formation of the clumps, rings, or meshworks during node condensation as the strength of cross-linking is varied through parameter α. Video 7 and the snapshots in Figure 5G for three values of α closely match the phenotypes observed in cross-linker deletion mutants, wt, and Ain1 overexpression
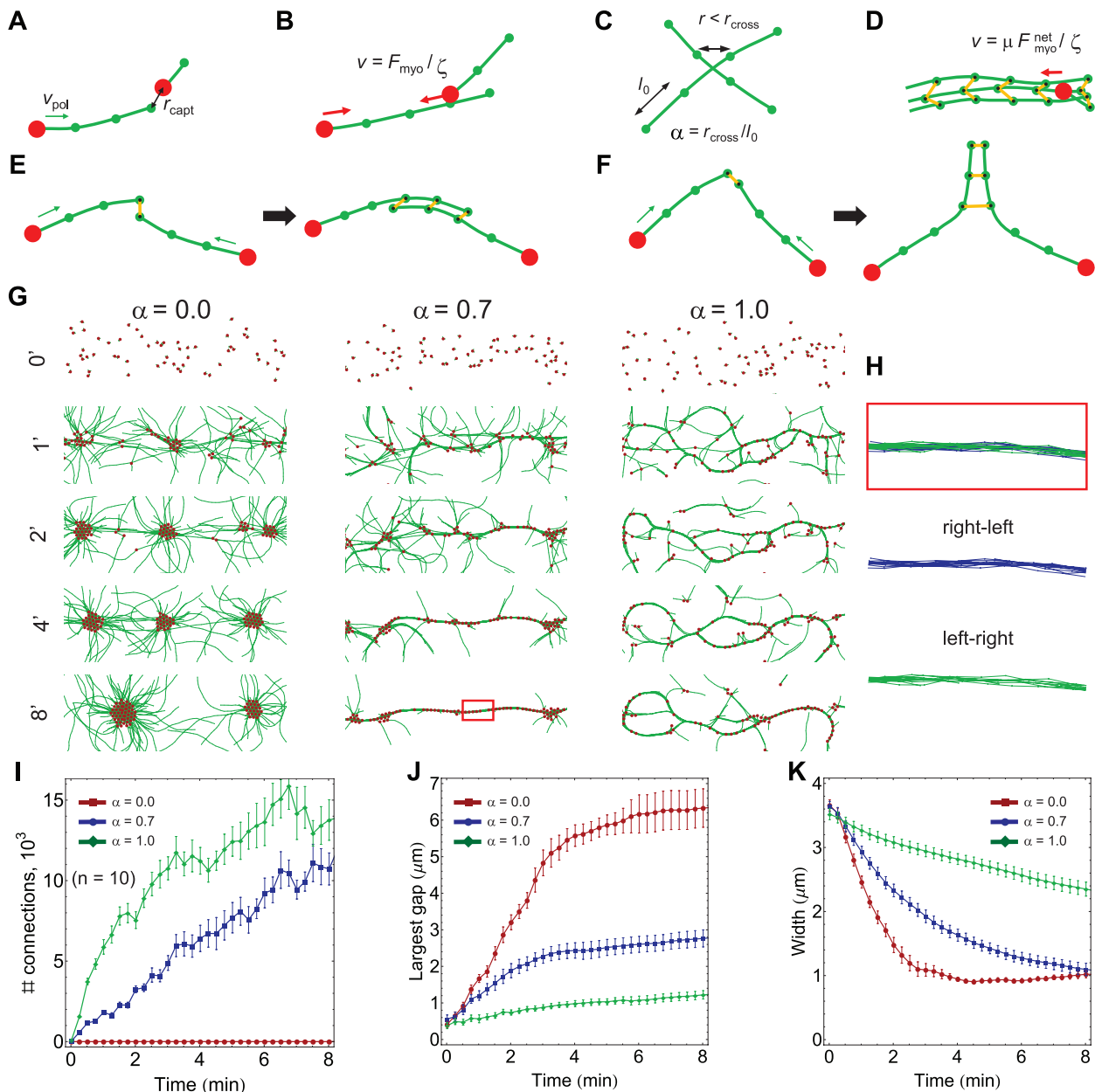
FIGURE 5: Model of SCPR with actin filament cross-linking explains clump and meshwork structures in cross-linker mutants. (A–F) Summary of basic processes. (A) Search and capture: actin filaments (green; represented as beads connected by springs of equilibrium length l_0) polymerize out of nodes (red) with velocity v_{pol} (the barbed ends of filaments are assumed to associate with formins at nodes). Actomyosin connections are established when filament beads come within r_{capt} to the other node. Filament lifetime is t_{turn} ("release"). (B) Pull: nodes bound to a filament exert force F_{myo} toward the barbed end of the filament at the nucleating node. The force is transmitted through the filament and results in node pair-wise movement with velocity $v = F_{myo}/\zeta$. (C) Cross-linking occurs when two actin filament beads are within distance r_{cross} of one another (represented by an interaction potential between beads). (D) Nodes that establish multiple actomyosin connections inside an actin bundle exert lower total force per filament. (E and F) Depending on the angle of intersection, growing filaments can align into antiparallel (E) or parallel (F) bundles. (G) Snapshots of two-dimensional simulations of node condensation for different values of parameter $\alpha = r_{cross}/l_0$. Cases $\alpha = 0$ (no cross-linking, similar to *ain1Δ fim1Δ* cells), 0.7 (moderate cross-linking as in wt cells), and 1 (excessive cross-linking as in Ain1p overexpression cells) show formation of clumps, rings, and meshworks, respectively. Times are in minutes. Also see Video 7. (H) Snapshots of actin filament arrangements in the red box in G ($\alpha = 0.7$, 8 min). The bundle consists of both parallel and antiparallel filaments: blue (green) indicates filaments the barbed-to-pointed end direction of which is toward the left (right). (I) Total number of actin filament bead cross-links vs. time, and α shows a trend similar to experiments (Figures 1C and 2A). (J) Largest gap vs. time and α. Absence of cross-linking results in disconnected node aggregates, similarly to experiments, see Figure 1, D and F. (K) Increased cross-linking slows down condensation. Node band width vs. time and α. Band width is calculated as 4 SDs of *y* node coordinates, which approximately corresponds to the width measured in Figure 4A. Error bars in all graphs are SEM ($n = 10$ simulations).
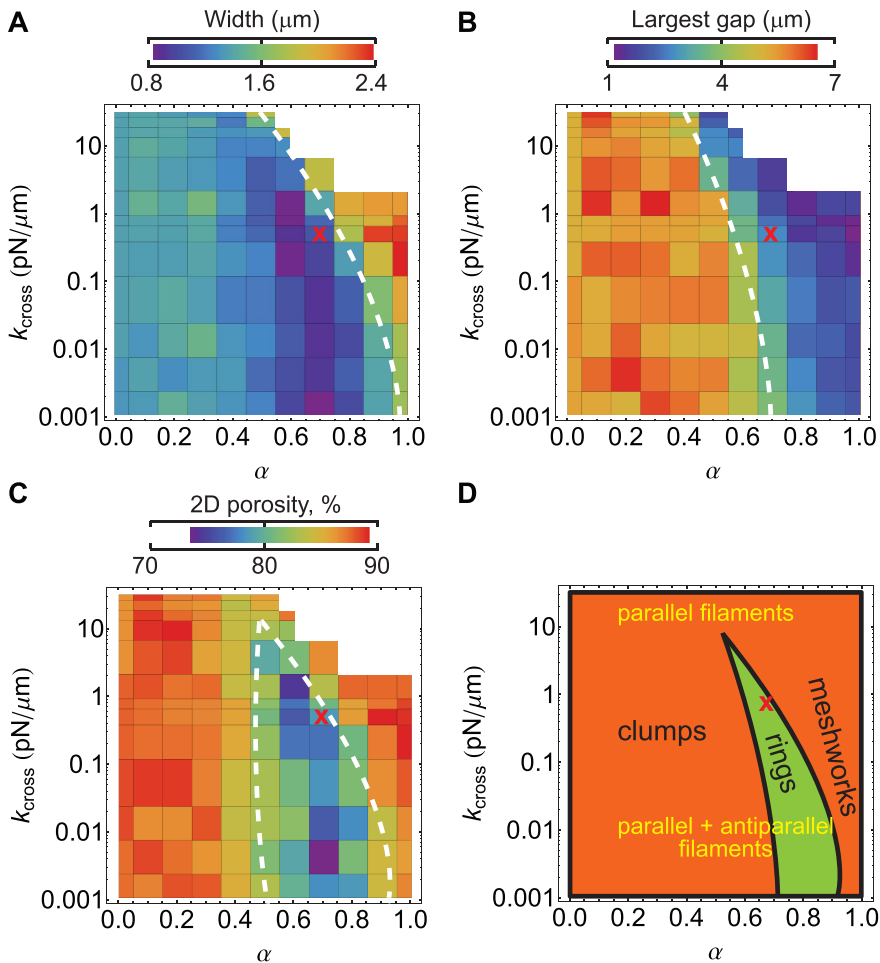
FIGURE 6: Dependence of node aggregate structures on cross-linker model parameters. (A–C) Width, largest gap, and two-dimensional porosity vs. α and k_{cross}, calculated 500 s after the start of simulation (mean of 10 runs). Dashed lines separate physiological from nonphysiological regions. White area: cross-linking is too strong for meaningful simulations. Red X: parameters used in Figure 5G, wt case. The α-dependence for small k_{cross} is due to our use of α in counting actin filaments in a bundle and resulting reduction of myosin pulling (Figure 5D). (D) Summary of preceding panels showing region with successful ring formation.

cause of the stabilizing effect of cross-linking, the assumption of force-induced reduction of polymerization rate of the original SCPR model was not as important in preventing clumps (Supplemental Figure S7A).

The full dependence of resulting node aggregation on model parameters α and k_{cross} in Figure 6 illustrates how cross-linker properties lead to different cytoskeletal organization and recapitulates our in vivo observations. Fission yeast may have optimized cross-linker concentration and rate constants to lie in the functional region of parameter space. Our simulations thus support a mechanism in which actin cross-linking aligns actin filaments within transient bundles, which in turn define how nodes condense.

Successful node condensation is a cooperative process between myosin II and actin cross-linkers

Our numerical simulations show that node condensation is a cooperative process in which the actin network and nodes affect each other. Without myosin pulling, actin cross-linking in the model does not provide enough force to pull nodes together, resulting in a transient meshwork structure of actin filaments (Figure 7, A and B). Consistent with prior reports (Coffman *et al.*, 2009; Stark *et al.*, 2010), we found that *myo2-E1* cells with defective Myo2 motor activity could not condense nodes and the actin network into a contractile ring, forming instead a dynamic meshwork similar to the simulations (Figure 7C).

When $\alpha = 1$, cross-linking slows node movement induced by myosin pulling (Figure 5, G and K). We predict that sufficiently high myosin-pulling forces can overcome the restriction imposed by cross-linking activity and condense actomyosin meshworks into rings in Ain1 overexpression cells (Figure 8, A and B). With lower levels of cross-linking in the simulations, higher myosin-pulling force condenses nodes into clumps or rings at a faster rate compared with wt (Figure 8A). We performed experiments to test the predictions. We expect that increasing myosin concentration increases the node-pulling force, because nodes condense into a compact ring twofold faster in cells with two copies of the *myo2* gene (Stark *et al.*, 2010). Therefore we overexpressed Myo2 in cells expressing different levels of cross-linkers. In this background, Myo2 quantity increased approximately twofold in the broad band of nodes (Supplemental Figure S9, A and B), whereas node numbers stayed constant compared to wt cells (Supplemental Figure S9C). Thus the level of myosin heavy chain concentration per node doubles. As predicted by the simulations, in *2x myo2 41nmt1-ain1* cells, nodes condensed more normally, with less tilted/double rings compared with *41nmt1-ain1* cells (Figure 8C; Video 8). The overall node condensation rate was 106 nm/min in *2x myo2 41nmt1-ain1* cells, compared with 206 nm/min in wt and 53 nm/min in *41nmt1-ain1* cells (Figure 8D). Consistent with prior reports (Stark *et al.*, 2010), we found

cells. Clumps form without cross-linking ($\alpha = 0$). This clump formation was enhanced compared with the original SCPR model (that does not include cross-linkers) by allowing filaments to make contact with multiple nodes (Vavylonis *et al.*, 2008). In the simulations that correspond to wt cells ($\alpha = 0.7$), alignment of nodes through cross-linked actin filaments prevents them from coalescing into clumps. However, this alignment is transient and does not trap nodes into stable linear meshwork structures, as observed when growing filaments are strongly cross-linked ($\alpha = 1$). When nodes condense into rings, the rings consist of bundles of antiparallel filaments (Figure 5H).

The trend of the number of cross-linkers versus time in simulations (Figure 5I) matches experimental observations (Figures 1C and 2A). Figure 5J shows that gaps do not grow far above the diffraction limit for sufficiently high α whereas large gaps that correspond to the formation of two to three clumps develop for $\alpha = 0$, as in Figure 1, A and D. Plots of broad band width versus time (Figure 5K) match experimental observations (Figure 4A). Similar agreement is found for porosity and node movement statistics (Supplemental Figure S6, B–D). The model can also successfully account for the formation of meshwork of intersecting bundles/double rings in *cdc25-22* cells (Ojkic *et al.*, 2011), using $\alpha > 0.7$ (Supplemental Figure S8A). Be-
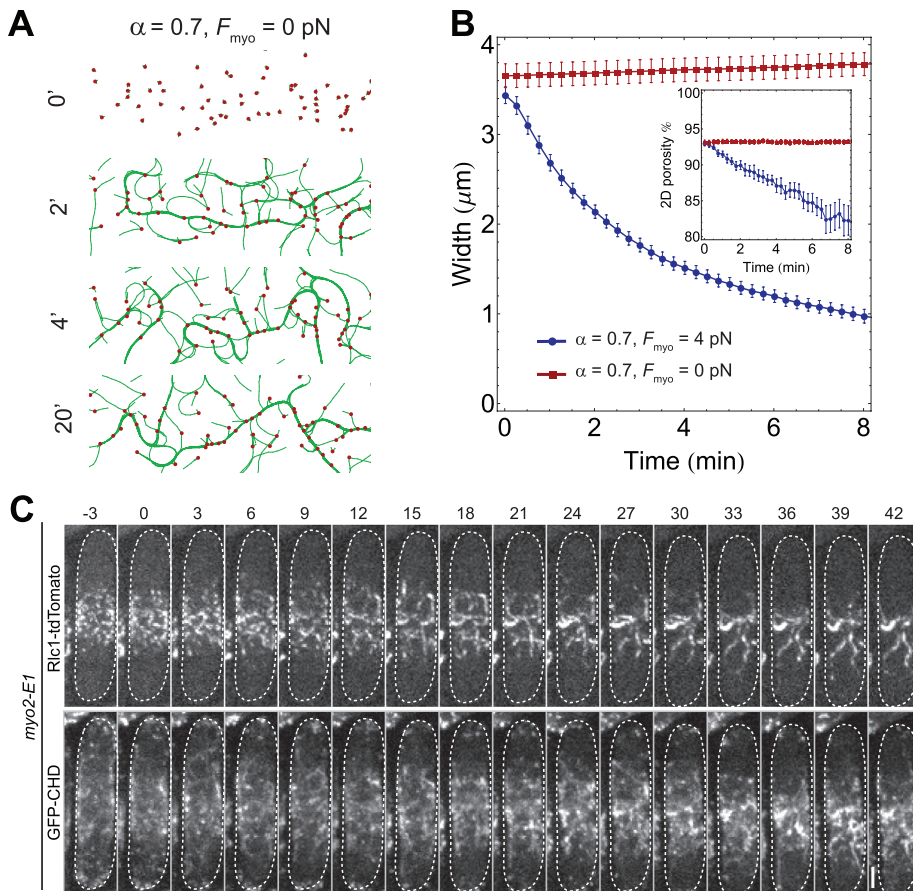
FIGURE 7: Myo2 activity is essential for node condensation. (A and B) Simulations including cross-linking but insufficient myosin motor activity predict meshwork of bundles that fail to condense into rings. (A) Snapshots show ring formation with $\alpha = 0.7$, $F_{myo} = 0$ pN. (B) Band width vs. time and F_{myo} with all other parameters fixed. Inset: two-dimensional porosity vs. time shows porous meshworks at small F_{myo}. (C) Rlc1 nodes form unstable linear structures with defective myosin II activity. Time courses of Rlc1-tdTomato and GFP-CHD localization in *myo2-E1* cells grown at 36°C for 2 h and imaged at 36°C. *41nmt1-GFP-CHD* was induced in EMM5S for 24 h at 25°C before shifting to 36°C.

The biochemical properties of Ain1 have not been characterized. However, we assumed that Ain1 is an actin cross-linking protein for the following reasons: 1) Ain1 co-localizes with actin filaments at the division site (Figure 3C) and the localization is actin dependent (Wu *et al.*, 2001); 2) the putative actin-binding sites within the ABD of Ain1 are >50% identical to chicken α-actinin, which is known to have actin cross-linking activity (Xu *et al.*, 1998); and 3) we find that the spectrin-like repeats of Ain1 are important for its function (Supplemental Figure S9D), presumably for dimerization (Djinovic-Carugo *et al.*, 1999). Thus it is highly likely that Ain1 is an actin cross-linking protein.

We found that α-actinin Ain1 and fimbrin Fim1 regulate node condensation but do not affect node formation or initial distribution. Starting from an approximately Gaussian distribution along the long cell axis, nodes execute a biased random walk toward the cell equator. In the process, they align into transient linear structures that form stochastically as revealed by our experiments and reproduced by computational simulations. Without the cross-linkers, these linear structures are unstable and collapse into clumps that attract surrounding nodes. By contrast, nodes condense into numerous linear structures that form meshworks when Ain1 is overexpressed. This stabilization of actin cytoskeleton by α-actinin is consistent with a mammalian α-actinin study (Mukhina *et al.*, 2007).

Importance of cross-linker dynamics and cross-linking orientation

An important assumption in our simulations was the fact that cross-linking activity (described by parameters α and k_{cross}) is dynamic. This allows actin filaments to slide past one another as they polymerize. In our simulations, the resistance force per $l_0 = 0.2$ µm of two actin filaments polymerization at 100 nm/s against one another as in Figure 5E is of order $\alpha k_{cross} l_0 \approx 0.07$ pN. At that speed, the drag force by an α-actinin molecule in vitro is estimated to be 0.012 pN (Greenberg and Moore, 2010), thus corresponding to a few α-actinin molecules per micron of actin filaments in our simulations. With these numbers, the total amount of cross-linkers in simulations is close to that measured in experiments. This finding indicates that our chosen values for α and k_{cross} are realistic.

We note that the FRAP recovery rate of α-actinin in stress fibers (Swartz, 1999; Edlund *et al.*, 2001) is much slower than the dissociation rate of α-actinin from actin filaments in vitro (Xu *et al.*, 1998; Strehle *et al.*, 2011). This is likely due to the presence of two binding sites per α-actinin dimer and possible kinetic trapping of cross-linkers within actin bundles (Courson and Rock, 2010). Thus, during fission yeast contractile-ring formation, α-actinin Ain1 may allow actin filaments to rearrange considerably over times that are much shorter than our observed Ain1 recovery time in FRAP.

Another important factor in the simulations was the ability of antiparallel cross-linking. Fim1 bundle actin filaments in both parallel

that *2x myo2* cells condense nodes faster to form a contractile ring, similar to the simulations (Figure 8E). In *ain1Δ*, 49% of cells displayed clump formation during mEGFP-Myo2 node condensation (Figure 8E; $n = 41$). Interestingly, all *2x myo2 ain1Δ* cells formed clumps ($n = 38$; Figure 8E). Together these results indicate that node condensation into the contractile ring is a cooperative process in which myosin II and actin cross-linkers affect each other.

DISCUSSION

Actin cross-linkers modulate and organize actin filaments during contractile-ring assembly

In fission yeast, the actomyosin ring assembles through the condensation of the cytokinesis nodes and actin filaments. Previous experiments and numerical simulations suggest that actin filaments nucleated from nodes establish transient actomyosin connections among them, leading to node condensation into a ring (Wu *et al.*, 2006; Vavylonis *et al.*, 2008; Coffman *et al.*, 2009). Here we revealed actin cross-linkers α-actinin Ain1 and fimbrin Fim1 to be two additional important players in the process of node condensation. We showed that these proteins help align the condensing nodes into a ring by stabilizing transient linear structures.
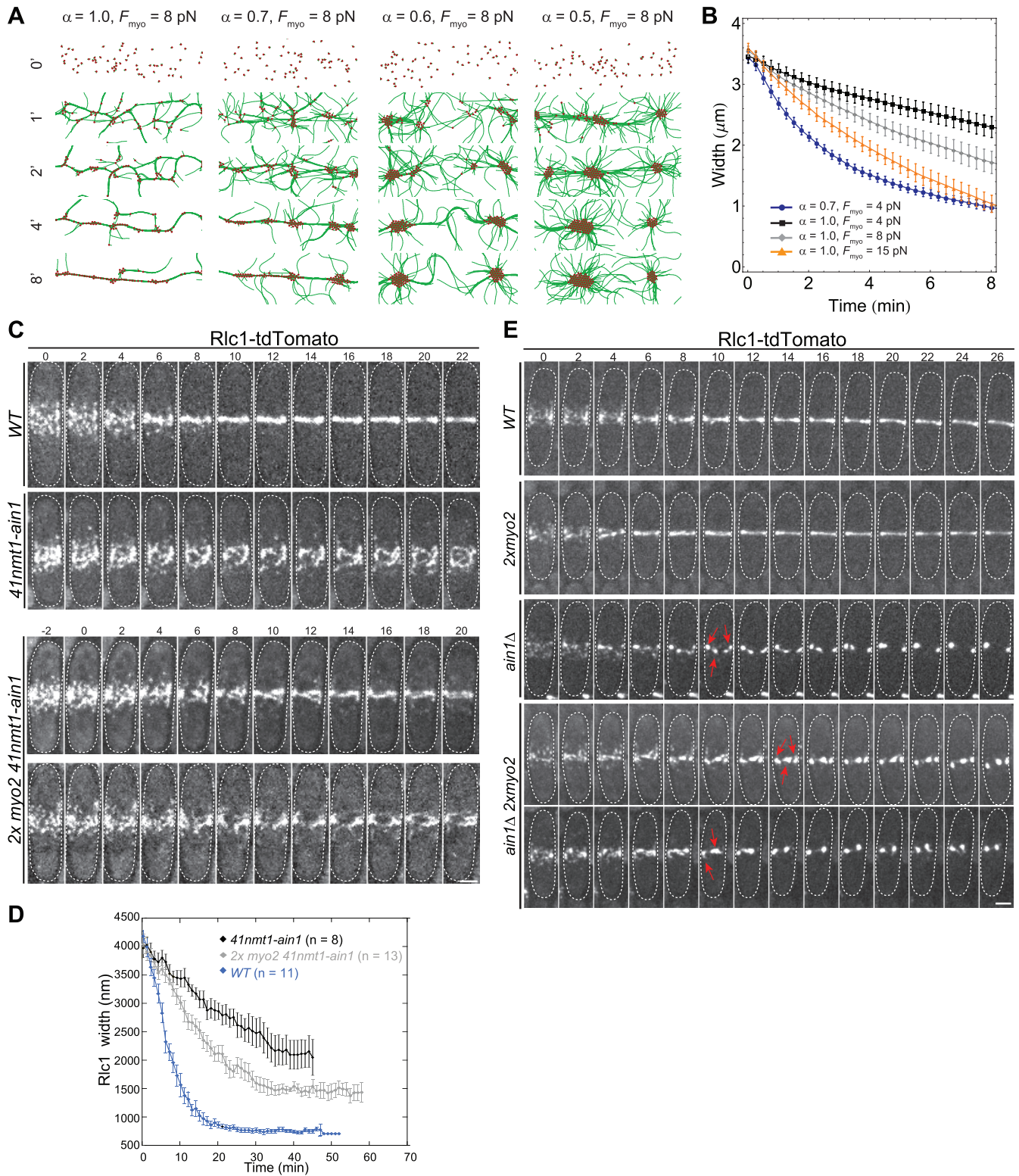
FIGURE 8: Cooperation between Myo2 activity and Ain1 cross-linking during node condensation: comparison of model predictions to experiments. (A) Simulation snapshots with myosin pulling force F_{myo} = 8 pN, increased compared with Figure 5 where F_{myo} = 4 pN. Nodes condense into rings without frozen meshworks for α = 1. For α < 0.7, clumps always form. (B) Simulated band width (measured as in Figure 5K) vs. time and F_{myo}, keeping other parameters fixed. Plot shows faster condensation with increasing F_{myo}. Error bars are SEM (*n* = 10 simulations). (C and D) Doubling Myo2 level partially rescues the ring-formation defect in Ain1 overexpression cells. (C) Time courses of Rlc1 localization in wt, *41nmt1-ain1*, and two representative *2x myo2 41nmt1-ain1* cells (also see Video 8). Strains were grown 22 h in EMM5S. (D) Width of Rlc1 broad band over time (mean ± SEM). (E) Doubling myosin II level increases clump formation in *ain1Δ*. Time courses of Rlc1-tdTomato localization in wt, *2xmyo2*, *ain1Δ*, and two representative *2xmyo2 ain1Δ* cells. Red arrows indicate clump formation. (C and E) Times are in minutes. Bars, 2 μm.

and antiparallel orientations (Skau et al., 2011), and α-actinin is known to have this ability in other cell systems (Meyer and Aebi, 1990; Courson and Rock, 2010), both consistent with the assumption in our simulations. With this assumption, the simulations reveal that different filament orientations may prevail depending on system parameters. Actin filaments that grow out of clumps are cross-linked in a parallel manner, whereas those that link linear node structures have both parallel and antiparallel orientations. These different organizations of actin filaments in different cells may explain both node-dependent and -independent pathways for contractile-ring formation (Kamasaki et al., 2007; Roberts-Galbraith and Gould, 2008; Pollard and Wu, 2010).

The simulations highlight the role of Ain1, but more work is needed to understand the role of Fim1. The fact that mild Fim1 overexpression rescues the Ain1 deletion phenotype suggests similar functions, despite possible differences in the cross-linking geometry. Our simple treatment of cross-linking in the simulations that did not distinguish between Fim1 and Ain1 may thus still capture the main contributions of both proteins. However, Fim1 and Ain1 overexpression have different phenotypes, possibly due to different effects of these proteins on actin turnover (see discussion below).

System-level regulations by actin filament binding proteins

α-Actinins have been implicated in cytokinesis in different organisms. They localize to cleavage furrows in both fungi and animal cells (Fujiwara et al., 1978; Mabuchi et al., 1985; Sanger et al., 1987; Wu et al., 2001; Mukhina et al., 2007; Wang et al., 2009) to regulate actin dynamics and control the rate of furrow ingression (Mukhina et al., 2007). Fimbrins localize to cleavage sites and are involved in contractile-ring formation and furrow ingression by establishing a local tension on the actin network (Nakano et al., 2001; Wu et al., 2001; Shirayama and Numata, 2003; Reichl et al., 2008; Skau and Kovar, 2010). Although α-actinin regulates furrow ingression in mammalian cells, the rate of ring constriction in fission yeast is normal in ain1Δ or fim1Δ mutant (our unpublished data). Thus Ain1 and Fim1 are more important for the contractile-ring formation in fission yeast cytokinesis.

The results in this article further indicate the importance of cell-wide cytoskeletal regulation by actin filament side-binding proteins. These proteins regulate the length and dynamics of actin filaments that are critical parameters for contractile systems. Skau and Kovar (2010) found that tropomyosin Cdc8 protects actin filaments from the severing activity of cofilin. Interestingly, they showed that Fim1 competes with Cdc8 for actin filament binding. Our Fim1 overexpression results showing that nodes fail to condense because actin fails to concentrate to the equator at significant levels are consistent with this finding: a significant increase in fimbrin levels may displace Cdc8 from actin filaments and from cofilin severing activity; Fim1 overexpression may also stabilize actin filaments in actin patches and deplete the pool of free actin monomers. As a consequence of those two effects, shorter actin filaments will be nucleated/elongated by formin Cdc12 at the cell equator, resulting in failure of node condensation.

We found that Ain1 overexpression reduces the rate of actin turnover. We speculate that this decrease in the turnover rate could be due to a reduction of actin severing by cofilin or due to trapping of actin filament fragments inside bundles. The actin turnover rate in the simulations in Figure 5 was kept constant as parameter α was varied. We tested the effect of a cross-linking–induced reduction of actin turnover in Supplemental Figure S8 (B and C). Simulations still produced rings when the polymerization rate was simultaneously decreased to maintain constant F-actin concentration during the

late stages of ring formation, as observed in our experiments (see Supplemental Figure S5). A recent study showed that cells with defective cofilin condense nodes into clumps, as expected from simulations of the SCPR model with long-lived actin filaments (Chen and Pollard, 2011). Clearly, mutations of a single actin regulator can influence multiple aspects of actin dynamics. Future quantitative studies of actin turnover in cells will help to better indicate how the values of the parameters of our coarse-grained SCPR model (modified by the addition of cross-linking here) change in response to mutations of actin regulators.

Collectively our results support a cooperative process of contractile-ring self-organization involving components drawn together from distant parts of the cell, followed by a progressive and crucial stabilization that depends on actin cross-linking proteins.

MATERIALS AND METHODS

Strains, growing conditions, and cellular methods

Table S1 lists the *S. pombe* strains used in this study. All tagged genes are under the control of either endogenous promoters or *nmt1* promoters (with different strengths) integrated at their native chromosomal loci (Bähler et al., 1998b). Cells were grown in liquid YE5S medium at exponential phase at 25°C before microscopy except where noted. The media had no obvious effect on Ain1 expression level under its endogenous promoter. Global cytoplasmic concentration of Fim1 is ~24 times higher than that of Ain1 (Wu and Pollard, 2005), so *nmt1* promoters change their expressions to different degrees relative to the endogenous levels. To induce *nmt1* promoters, cells were grown in YE5S medium for 24 h, washed four times in EMM5S medium, and then grown for indicated times in EMM5S before microscopy. To repress *41nmt1-fim1* expression, cells were grown in EMM5S for 24 h, washed four times in YE5S, and then grown in YE5S + thiamine at 5 µg/ml for 22 h before microscopy. Cells in some experiments were synchronized by growing exponential cultures with 20 mM hydroxyurea (Sigma-Aldrich, St. Louis, MO) for 4 h at 25°C, washing twice with YE5S medium, and then resuming the cell cycle in YE5S for 1.5 h before imaging at 24–25°C. Unsynchronized temperature-sensitive strains were grown for 2 h at 36°C in YE5S and imaged on agar pads at 36°C. Diploid strains were constructed using standard genetic methods (Moreno et al., 1991) by crossing two Rlc1-tandem Tomato (tdTomato) haploid strains (with other mutations to be tested) containing complementary adenine mutation *ade6-M210* or *ade6-M216*.

Microscopy and data analysis

Live cell microscopy was performed as described (Coffman et al., 2009; Laporte et al., 2011; Ye et al., 2012) at 24-25°C, except where noted, using a thin layer of EMM5S liquid medium with 20% gelatin (Sigma-Aldrich) and 0.1 mM n-propyl-gallate. An objective heater (Bioptechs, Butler, PA) was used to maintain 36°C or other temperatures for microscopy of some temperature-sensitive mutants. For imaging, we used a 100×/1.4 NA Plan-Apo Nikon objective lens on a spinning disk confocal microscope (UltraVIEW ERS; Perkin Elmer Life and Analytical Sciences, Waltham, MA) with 440-, 488-, 514-, and 568-nm lasers and an ORCA-AG camera (Hamamatsu, Bridgewater, NJ). Except strains with GFP-CHD (no binning), all the images were taken with 2 × 2 binning.

Images were analyzed using ImageJ (http://rsb.info.nih.gov/ij/). Images in figures are maximum-intensity projections of z sections spaced at 0.2–0.4 µm except where noted. Radial projections of the cylindrical surface of the cell along the cell equator and 90° rotations were done using ImageJ plugin Radial4D and Projector 4D Float, respectively. Images in Figure 3, B and C, are

maximum-intensity projections of three *z* sections spaced at 0.25 μm after deconvolution using AutoQuant X2 software (Media Cybernetics, Bethesda, MD).

Porosity and largest gap measurements

To measure two-dimensional porosity (which differs from the one-dimensional porosity defined in Vavylonis *et al.*, 2008) and the largest gap of the contractile ring over time, the offset and uneven illumination were subtracted and corrected from movies, respectively (Wu *et al.*, 2008). Radial projections were made from movies with 21 slices at 0.2-μm spacing per min. Signals on radial projections were defined using a threshold 1.65 times higher than the cytoplasmic background using similar areas. Similar results were obtained using different thresholds. The percentage of pixels above the threshold was determined over time using ImageJ software. Two-dimensional porosity was defined as: 100 – measured percentage. To measure the largest gap in the contractile ring, the radial projections with the same threshold were converted into binary images (i.e., pixel below the threshold is zero, above the threshold is 255). Using plot profile in ImageJ, we measured the mean intensity for each column of pixels along the long cell axis in images. The maximum lengths of pixels with zero intensity were determined and converted into nanometers.

Node displacement measurement

The top of the cell (three to five planes) was imaged to follow the nodes in the same focal plane. Individual node movements were tracked in movies (10-s delay) using the plug-in MTrackJ in ImageJ. Four parameters were extracted: node displacement, instantaneous node speed, movement frequency, and angle of displacement. Node displacement is the straight line distance between node positions at the beginning and end of a specified time period. Instantaneous node speed is the actual distance traveled by a node per second. Movement frequency is the percentage of instantaneous node speeds >10 nm/s divided by the numbers of all the instantaneous node speeds measured. Angle of displacement is the angle from the line formed by initial and end positions of the node to the long cell axis. Using node coordinates, angle (θ) was determined using the equation $c^2 = a^2 + b^2 - 2ab \cos\theta$.

Node distribution and condensation analyses

We used the full width at half maximum (FWHM) to determine the node distribution along the long cell axis before node condensation. We drew a box of 5.3×4.2 μm^2 around the band of nodes in maximum intensity projection. Mean intensity in each pixel column perpendicular to the long cell axis was obtained using plot profile in ImageJ and fit with the Gaussian equation in KaleidaGraph (Synergy Software, Reading, PA). Using σ (SD) predicted by the Gaussian equation, individual FWHM values were calculated as follows: FWHM = 2 √(2 * ln2) * σ ≈ 2.355 * σ. The Gaussian distributions of node intensity were manually aligned using the calculated centroid of each distribution, and then the relative mean intensities were plotted.

We estimated the global node condensation rate over time by measuring the width of Rlc1 or Myo2 node distribution along the long cell axis. After subtracting background, correcting for photobleaching during image acquisition, and rotating cells to align their long axis with the *y*-axis, the width of Rlc1 or Myo2 signals along the *y*-axis was measured using a rectangle region of interest (ROI) by setting a threshold twofold higher than the cytoplasmic background near the cell tip. Individual widths were manually aligned at time 0.

Counting Ain1 molecules over time

We counted Ain1 molecules based on fluorescence intensity (Wu and Pollard, 2005; Wu *et al.*, 2008; Laporte *et al.*, 2011) with some modifications. For intensity comparison, images were collected using the same laser power and imaging settings. We previously determined that the FWHM of the point spread function for our confocal system is 0.39 ± 0.02 μm along the *z*-axis (Coffman *et al.*, 2011; Laporte *et al.*, 2011). Thus, to avoid oversampling Ain1 signals, we collected *z* sections spaced at 0.4 μm for Ain1 strains. Strains were imaged in the presence of wt strain JW740 to correct for cellular autofluorescence. Offset intensity, uneven illumination, and photobleaching during image acquisition were corrected (Laporte *et al.*, 2011). Then, 11 *z* sections from each time point were summed. Ain1 intensities in the entire cell or at the division site were measured using polygon ROIs in ImageJ.

To obtain the numbers of Ain1 molecules over time, we used the previously determined Ain1 global concentration (0.22 μM) as a standard (Wu and Pollard, 2005), giving a total of 4923 Ain1 molecules in wt mitotic cells with a mean volume of 126 μm^3. Given that wt Ain1 global concentration in the cell does not change over time (Wu and Pollard, 2005), we obtained the number of Ain1 molecules by the following formula: (4923 * intensity$_x$) / (mean cell intensity of wt Ain1), where intensity$_x$ was Ain1 intensity either in the whole cell or at the cell equator. Mean Ain1 cell intensity was 98,262 (*n* = 20 cells). Measurements for Ain1 in the entire cell or at the division site in overexpression strains were obtained the same way.

Analyses of actin cytoskeleton dynamics

We first used a low dose of Lat-A to study actin dynamics. Cells were washed in EMM5S with 0.1 mM *n*-propyl-gallate and preincubated with 100 μM Arp2/3 inhibitor CK-666 (Chemdiv, San Diego, CA; Nolen *et al.*, 2009) for 5 min to reduce the interference of actin patches for analysis. Then, 10 μM Lat-A was added, and cells were imaged immediately on bare slides. Here time 0 is the start of the observation. Intensities in 12 *z* sections spaced at 0.35 μm for each time point were summed. GFP-CHD intensities at the division site were measured using polygon ROIs in ImageJ, and background corrections were made using a concentric ROI twice as big as the GFP-CHD ROI (Wu *et al.*, 2008). After subtracting background and correcting for photobleaching during image acquisition, intensity values at each ROI were normalized against the fluorescence intensity at time 0, which is set to 100%. Curve fits were obtained from the mean of all cells. SDs were obtained from individual measurements. The single exponential decay curve equation is $y = m1 - m2 * \exp(-m3 * x)$, where m_3 is the off rate. To calculate the $t_{1/2}$ of the decay, we used the equation $t_{1/2} = \ln2/m_3$. To get a plateau for each decay curve, images were collected in 30-s intervals over 10–15 min.

We also tested the dynamics of the actin cytoskeleton by comparing GFP-CHD images (Figure 3, D and E). The top of the cell (five *z* sections spaced at 0.2 μm with a 10-s delay between stacks) was imaged to follow actin filaments over time. Images were subtracted for cytoplasmic background and corrected for uneven illumination. Two successive stacks were summed and converted to binary (0 and 255) using a threshold set at a pixel intensity 2.5-fold higher than that of the cytoplasmic background (containing no GFP-CHD filaments). Image stacks separated by 40 s were used to measure similarity (T_x and T_{x+40}). Custom software written in MatLAB R2009 (MathWorks, Natick, MA) was used to convert all pixels with 0 in T_{x+40} to 1. Next T_x was subtracted by T_{x+40} to determine four variables: the number of pixels with unchanged GFP intensity (0), the number of pixels in which GFP signal disappeared (254), the number of pixels in which GFP signal appeared (–255), and the number of

pixels unchanged as background (–1). Note that converting all pixels with 0 in T_{x+40} to 1 allows us to distinguish background pixels from pixels with GFP-CHD signals during similarity measurements. Similarity percentage was defined as the number of pixels with unchanged GFP intensity / (total pixels – background pixels).

FRAP analysis

We used the Photokinesis unit on the UltraVIEW ERS confocal system for all FRAP assays (Coffman et al., 2009). The FRAP data were obtained and analyzed as described (Laporte et al., 2011). Briefly, curve fits were obtained from the mean of all ROIs. SDs were obtained from individual ROIs. The single exponential curve equation is $y = m_1 + m_2 \exp(-m_3 x)$, where m_3 is the off rate. The off rate was used to calculate the $t_{1/2}$ of the recovery using the equation $t_{1/2} = \ln 2 / m_3$. To obtain a plateau for each mEGFP-Ain1 recovery curve, images were collected with 2.5-s intervals.

Western blotting

Protein extracts were prepared from log-phase cells grown in EMM5S liquid medium for the indicated times. Approximately 2 × 10^8 cells were collected, rinsed in ice-cold phosphate-buffered saline (PBS; 137 mM NaCl, 2.7 mM KCl, 4.3 mM Na$_2$HPO$_4$, 1.47 mM KH$_2$PO$_4$, pH 7.4) + 1 mM phenylmethylsulfonyl fluoride (PMSF), and frozen at –80°C. Cells were lysed in 125 μl of lysis buffer (50 mM HEPES, pH 7.6, 75 mM KCl, 1 mM MgCl$_2$, 1 mM EGTA, 0.1% Triton X-100, and 1 mM dithiothreitol [DTT]) with protease inhibitors (10 μl of protease inhibitor cocktail [Sigma P8215], 1 mM PMSF, 1 mM sodium vanadate, 20 mM β-glycerophosphate) with 500-μl glass beads (425–600 μm, Sigma G8772). New lysis buffer (275 μl) was added to the lysate, and the extracts were centrifuged twice at 14,000 rpm at 4°C. Sample buffer was added to the supernatants, and the samples were boiled for 5 min. Immunoblotting was performed as described (Laporte et al., 2011). The following antibodies were used: mouse anti-myc antibodies (9E10, Covance; dilution 1:10,000), mouse anti-GFP antibody (Roche, Indianapolis, IN; dilution 1:500), mouse anti-hemagglutinin (HA) antibody (Sc-7392; Santa Cruz Biotechnology, Santa Cruz, CA; dilution 1:400), and chicken anti-yeast actin antibodies (a generous gift from B. Goode [Brandeis University, Waltham, MA], dilution 1:3000). Blots were detected with SuperSignal Wes Pico (34077; Thermo Fisher Scientific, Waltham, MA).

Actin staining using phalloidin

Cells were cultured in EMM5S liquid medium for the indicated times and then fixed for 1 h at 30°C with 1/3 volume of 16% paraformaldehyde (Sigma P-6149) dissolved in PEM buffer (100 mM 1,4-piperazinediethanesulfonic acid sodium salt [PIPES], 1 mM EGTA, 1 mM MgSO4, pH 6.9). After fixation, cells were washed three times with PEM, once with PEM with 1% Triton for 30 s, and then three more times with PEM.

Alexa Fluor 488/568 phalloidin (7 μl; Invitrogen, Carlsbad, CA, A12379 and A12380) were evaporated using a SpeedVac, resuspended in PEM buffer, and added to 1 μl of concentrated fixed cells. Cells were incubated for 30 min at room temperature and overnight at 4°C. Before imaging, cells were washed once in PEM and imaged in PBS-glycerol mounting medium containing one flake of p-phenylenediamine (Sigma P-6001).

Construction of Ain1 with zero spectrin-like repeats (SRs)

We constructed Ain1 with zero SRs using a mutagenesis method described previously (Lee and Wu, 2012). The ain1 gene has two introns (51 and 140 base pairs in length) within the region encoding the ABD. The fragments used for constructing Ain1 with 0 SRs are downstream of the introns. Thus the sequences and positions mentioned later in this section correspond to ain1 cDNA sequences (total 1866 base pairs for 621 aa). First, we amplified an ain1 fragment from 550 to 1866 base pairs, containing the encoding sequences for SR1 and SR2 (733–1431), the EF Hand motif, and some flanking sequences. We cloned the fragment into the TOPO vector (3.5 kb) to obtain plasmid JQW238. To delete the two SRs for constructing Ain1::0SR, we used two primers (forward primer WU531, 5′ AAGAGAACACTCTCCAAACAAGAACTAGAC-3′ and reverse primer WU532, 5′ CCTCTCTACACGTCTAGCCGCAGTTTCCAC-3′) with their 5′ ends (1432 and 732) separated by the two SR sequences to amplify JQW238 using iProof DNA polymerase. The PCR product was blunt-end ligated using T4 DNA ligase. The resulting plasmid is JQW240, which was sequenced to verify no frame shift or mutations during the amplification process. Last, we deleted the SR1-SR2 in Ain1 in a wt strain using the ura4+ gene. Plasmid JQW240 was amplified in Escherichia coli and digested with SacI and XhoI to release ain1::0SR with the flanking sequences. The fragment was transformed into ain1-ΔSR1SR2::ura4+ cells. Transformants were selected on EMM5S + 5-FOA and then EMM5S – uracil. Selected cells were PCR checked for correct integration of ain1::0SR.

Description of computational model

Our simulations represent an approximate description of the system and include those mechanistic aspects that are the most important in determining the qualitative pattern of system behavior, namely its ability to form clumps, rings, and meshworks. We explicitly included crucial sources of variability (such as randomness) in initial node positions and filament orientations but approximated other sources of variability (such as fluctuations in node size and cytoplasmic viscosity) by averages. The robustness of our model to changes in model parameters is described later in the text, in Table S2, and in a previous publication (Vavylonis et al., 2008).

Actin filament representation and dynamics. Actin filaments are simulated two-dimensionally as strings of beads connected with springs of equilibrium length $l_0 = 0.2$ μm (approximately equal to the node size, the smallest scale, of relevance in the simulations). We used Langevin dynamics to solve for the position $\mathbf{r}_i(t)$ of the ith filament bead (Pasquali and Morse, 2002; Kim et al., 2009):

$$\zeta_b \frac{d\mathbf{r}_i}{dt} = \mathbf{F}_i^{spr} + \mathbf{F}_i^{bend} + \mathbf{F}_i^{stoch} + \mathbf{F}_i^{xlink} + \mathbf{F}_i^{myo}, \quad i \in \{1, 2, \ldots, N\} \quad (1)$$

Here N is the total number of beads and ζ_b is the drag coefficient of a filament segment of length l_0. For simplicity, we approximate the drag coefficient to be the same along all directions ($\zeta_b = \zeta_\perp = \zeta_\parallel$). To estimate ζ_b, we use $\zeta_\perp = 4\pi \eta \, l_0/[\ln(l_0/2a) + 0.84] = 0.216$ pN s/μm for a rod of length l_0 and radius $a = 3.5$ nm and $\eta = 350 \, \eta_{water} = 0.301$ Pa s as the cytoplasmic viscosity (Howard, 2001). The forces on the right hand side of Eq. (1) are as follows:

1. Spring force:

$$\mathbf{F}_i^{spr} = -\frac{\partial E^{spring}}{\partial \mathbf{r}_i} = -\frac{k}{2} \sum_{j=1}^{N-1} \frac{\partial (|\mathbf{r}_{j+1} - \mathbf{r}_j| - l_0)^2}{\partial \mathbf{r}_i}$$

This is the force by the neighboring springs, where E^{spring} is the total spring energy. We used a spring constant $k = 150$ pN/μm, a value large enough to maintain filament length but also small enough to allow small enough forces and thus use of large integration time steps (we note that this value is smaller than the value of the spring constant corresponding to the Young's module E of an actin filament, $k = E S / l_0 \approx 346 \cdot 10^3$ pN/μm, where S is the area of the actin filament cross-section (Kojima et al., 1994).

2. Bending force:

$$\mathbf{F}_i^{\text{bend}} = -\frac{\partial E^{\text{bend}}}{\partial \mathbf{r}_i} = \frac{\kappa}{l_0}\sum_{j=2}^{N-1}\frac{\partial(\mathbf{t}_j \cdot \mathbf{t}_{j-1})}{\partial \mathbf{r}_i}$$

is the force due to the elastic energy of bending, E^{bend} (Pasquali and Morse, 2002). Here

$$\mathbf{t}_j \equiv \frac{\mathbf{r}_{j+1} - \mathbf{r}_j}{|\mathbf{r}_{j+1} - \mathbf{r}_j|}$$

is the local unit tangent vector. The flexural rigidity κ in thermal equilibrium satisfies $\kappa = k_B T \, l_p$, where k_B is Boltzmann's constant, T is temperature, and $l_p = 10\,\mu m$ is the equilibrium persistence length (Gittes et al., 1993).

3. Random force: $\mathbf{F}_i^{\text{stoch}}$ represents the thermal and random active forces acting on the filaments. It enables exploration of a range of angles by fluctuations. We used

$$\langle \mathbf{F}_i^{\text{stoch}} \, \mathbf{F}_i^{\text{stoch}\,T}\rangle_{\alpha,\beta} = \frac{2k_B T \zeta_b}{\Delta t}\hat{I}_{\alpha,\beta}$$

where $\hat{I}_{\alpha,\beta}$ is the second order unit tensor, Δt is the simulation time step (Kim et al., 2009), and $T = 300$ K (thermal forces only). Our results do not change significantly by using a twofold larger effective temperature (Gallet et al., 2009). Use of even higher effective temperatures is possible, but this requires adjustments in κ and other parameters such that the effective persistence length of actin filaments that grow out of nodes is not less than ~3 μm and cross-linking is not disrupted by large random forces.

4. Force due to cross-linking:

$$\mathbf{F}_i^{\text{xlink}} = -\frac{k_{\text{cross}}}{2}\sum_j \frac{\partial(|\mathbf{r}_i - \tilde{\mathbf{r}}_j| - l_x)^2}{\partial \mathbf{r}_i}$$

where the sum is over all beads of other filaments at position $\tilde{\mathbf{r}}_j$ that are within r_{cross} of bead i. Thus, when bead i is within r_{cross} of bead j of another filament, we introduce an elastic interaction between the beads, with spring constant k_{cross} and natural length l_x (see Figure 5C). In Figure 5 we used $k_{\text{cross}} = 0.5$ pN/μm and $l_x = 0.05$ μm. Because l_x represents the average distance between two cross-linked actin filament segments, we used a value slightly larger than the length of the α-actinin dimer (Klein et al., 2004; Sjoblom et al., 2008). Values of l_x in the range 0–80 nm produced similar results. Parameters k_{cross} and $\alpha \equiv r_{\text{cross}} / l_0$ represent the effective strength and dynamics of cross-linking, and their importance is examined in Figures 5 and 6. This simple linear spring model is sufficient to illustrate the main qualitative changes in network morphologies as a function of degree of cross-linking. However, the precise location of these morphological transitions in parameter space may depend on additional affects such as nonlinear torques that lead to cooperative effects and geometric alignment that we do not include in the model.

5. Myosin pulling force: $\mathbf{F}_i^{\text{myo}}$. When a node captures the ith filament bead, myosin pulling force is exerted toward the barbed end of the filament (Vavylonis et al., 2008). See Capture and pull.

Actin polymerization out of nodes (search). Each node polymerizes two actin filaments in random directions on a two-dimensional plane, as expected from the presence of ~2–4 formin Cdc12 dimers per node (Wu and Pollard, 2005; Coffman et al., 2009; Laporte et al., 2011), and Cdc12 is an efficient nucleator (one filament per ~3 Cdc12 dimers in vitro; Scott et al., 2011). Formins polymerize actin monomers while remaining attached to the barbed end. Single filament polymerization out of nodes was simulated by increasing the equilibrium length of the spring that joins the node and the first filament bead (see Supplemental Figure S6A). The polymerization rate (the speed of length elongation of the first segment) was $v_{\text{pol}} = 0.1$ μm/s, the typical polymerization rate during early stages of cytokinesis (Coffman et al., 2009). When the length of the growing segment was larger than l_0, a new bead was introduced. In the main text the polymerization rate was constant, but we also ran simulations with polymerization rate decreasing linearly with force (compressing or extensional) applied to the filament bead on the polymerizing node, up to stall force $F_{\text{stall}}^{\text{pol}}$, as suggested (Vavylonis et al., 2008; see Supplemental Figure S7A).

We assume that each filament starts to grow at a random angle φ_{pol} (see Supplemental Figure S6A). To maintain that angle, we assume a restoring torque on the first bead by applying a force $F_1^{\text{rot}} = k_{\text{rot}}(\varphi_{\text{pol}} - \varphi_1)/l_0(t)$, where φ_1 is the current angle of the first bead of the filament, k_{rot} is a constant, and $l_0(t)$ is the length of the first segment. The direction of the restoring force was perpendicular to the direction of the axis of polymerization. A force of the same magnitude but along the opposite direction was exerted on the polymerizing node. Additionally, to enable rotation of the orientation of the polymerization axis, we allowed the axis of filament polymerization to rotate toward the current position of the first bead in response to the restoring torque, with rate $\dot{\varphi}_{\text{pol}} = -k_{\text{rot}}(\varphi_{\text{pol}} - \varphi_1)/\zeta_{\text{rot}}$, where ζ_{rot} is an orientational drag coefficient (so φ_{pol} is fixed in the limit of large ζ_{rot} values). In the simulations in the main text, we used $k_{\text{rot}} / l_0 = 10$ pN/rad and $k_{\text{rot}}/\zeta_{\text{rot}} = 10$ s^{-1}. With these values, the axis of polymerization can rotate due to forces by myosin and cross-linkers. In Supplemental Figure S7B, we examine the effects of ζ_{rot} and show that node condensation into a ring is not strongly influenced by the value of ζ_{rot}. This parameter controls the alignment of actin filaments along nodes and could represent a mechanism related to the process of actin compaction into a bundle during ring maturation (Vavylonis et al., 2008).

Capture and pull. When the distance between a filament bead and a node, r, is less than the capture radius $r_{\text{capt}} = 0.15\,\mu m$, an actomyosin connection is established (Vavylonis et al., 2008). The bead-node connection was simulated by introducing an elastic interaction between bead and node with spring constant $k_{\text{bead–node}} = 2$ pN/μm and equilibrium length 0 μm (see Table S2). On establishing a connection, the node exerts an additional pulling force on the filament bead of magnitude $F_{\text{myo}}^0 = 4\,pN$ (Vavylonis et al., 2008) directed toward the barbed end and tangentially along the filament. An equal and opposite force is exerted on the connected node. Nodes can establish only one connection with the same filament but are able to connect with many filaments. To limit the magnitude of pulling forces when nodes connect with bundles of filaments, we assume that the pulling force exerted on a filament bead is reduced by a factor that depends on the number of cross-links N_c of the bead with other filament beads, $F_{\text{myo}} = \mu F_{\text{myo}}^0 / N_c$, for $N_c \geq 1$. We used $\mu = 0.3$ (see model dependence on μ in Supplemental Figure S7C). This reduction in force represents the myosin force being distributed over many filaments and interference of myosin activity with actin cross-linkers.

Turnover and release. The average filament lifetime was $t_{\text{turn}} = 20$ s (Vavylonis et al., 2008) (thus the typical filament length was $t_{\text{turn}} v_{\text{pol}} = 2$ μm). In the simulations, each filament disappears with probability $\Delta t/t_{\text{turn}}$ every $\Delta t = l_0 / v_{\text{pol}}$, and a new filament starts to grow in a new, randomly chosen direction. Supplemental Figure S8 (B and C) examines the effect of reduction of turnover rate by cross-linking. Filament beads can disengage from nodes when the applied forces cause the node and connected filament bead to drift apart beyond r_{capt}.

Forces on nodes. The position of a node, $\mathbf{r}_{node}$, was found by solving $d\mathbf{r}_{node}/dt = \mathbf{F}_{node}^{total}/\zeta_{node}$, where the node drag coefficient was $\zeta_{node} = 400$ pN s/µm (Vavylonis *et al.*, 2008). The total force on the node, $\mathbf{F}_{node}^{total}$, is the sum of the following four forces:

1. Elastic forces transmitted through filaments polymerizing out of the node. We calculate these forces by treating the node as a bead of an actin filament (see spring and bending force in *Actin filament representation and dynamics* section earlier in the text).

2. Forces due to the elastic spring that connects the node to filaments that polymerized out of other nodes.

3. Myosin pulling force when nodes connect to actin filaments polymerizing out of other nodes. This force is of equal and opposite magnitude to the force that the node exerts on the actin filaments.

4. Force due to excluded volume interactions among neighboring nodes when two nodes are within 0.20 µm of one another, represented by a repulsive radial force of magnitude 80 pN (Vavylonis *et al.*, 2008).

Numerical integration. Nodes were distributed in a sufficiently long two-dimensional strip with a density of 65 nodes per 12 µm, according to a Gaussian distribution with SD = 0.9 µm (we varied the initial width in Supplemental Figure S7D). The positions of nodes and filament beads were calculated by integrating the equations shown earlier text using a time step of $\Delta t = 5 \times 10^{-4}$ s. We validated the simulations of actin as semiflexible filaments by checking that we obtained the correct persistence length, tangent correlation function, and curvature distribution in thermal equilibrium (Smith *et al.*, 2010). We also confirmed that the relaxation time of each Fourier mode of the simulated filaments was in agreement with the analytical results in Gittes *et al.* (1993).

REFERENCES
Bähler J, Steever AB, Wheatley S, Wang Y-l, Pringle JR, Gould KL, McCollum D (1998a). Role of polo kinase and Mid1p in determining the site of cell division in fission yeast. J Cell Biol 143, 1603–1616.

Bähler J, Wu J-Q, Longtine MS, Shah NG, McKenzie III A, Steever AB, Wach A, Philippsen P, Pringle JR (1998b). Heterologous modules for efficient and versatile PCR-based gene targeting in *Schizosaccharomyces pombe*. Yeast 14, 943–951.

Balasubramanian MK, Bi E, Glotzer M (2004). Comparative analysis of cytokinesis in budding yeast, fission yeast and animal cells. Curr Biol 14, R806–R818.

Banerjee S, Liverpool TB, Marchetti MC (2011). Generic phases of cross-linked active gels: relaxation, oscillation and contractility. EPL 96, 58004.

Barr FA, Gruneberg U (2007). Cytokinesis: placing and making the final cut. Cell 131, 847–860.

Bartles JR (2000). Parallel actin bundles and their multiple actin-bundling proteins. Curr Opin Cell Biol 12, 72–78.

Bendix PM, Koenderink GH, Cuvelier D, Dogic Z, Koeleman BN, Brieher WM, Field CM, Mahadevan L, Weitz DA (2008). A quantitative analysis of contractility in active cytoskeletal protein networks. Biophys J 94, 3126–3136.

Chang F, Drubin D, Nurse P (1997). cdc12p, a protein required for cytokinesis in fission yeast, is a component of the cell division ring and interacts with profilin. J Cell Biol 137, 169–182.

Chen Q, Pollard TD (2011). Actin filament severing by cofilin is more important for assembly than constriction of the cytokinetic contractile ring. J Cell Biol 195, 485–498.

Coffman VC, Nile AH, Lee I-J, Liu H, Wu J-Q (2009). Roles of formin nodes and myosin motor activity in Mid1p-dependent contractile-ring assembly during fission yeast cytokinesis. Mol Biol Cell 20, 5195–5210.

Coffman VC, Wu P, Parthun M, Wu J-Q (2011). CENP-A exceeds microtubule attachment sites in centromere clusters of both budding and fission yeast. J Cell Biol 195, 563–572.

Courson DS, Rock RS (2010). Actin cross-link assembly and disassembly mechanics for α-actinin and fascin. J Biol Chem 285, 26350–26357.

Djinovic-Carugo K, Young P, Gautel M, Saraste M (1999). Structure of the α-actinin rod: molecular basis for cross-linking of actin filaments. Cell 98, 537–546.

Edlund M, Lotano MA, Otey CA (2001). Dynamics of α-actinin in focal adhesions and stress fibers visualized with α-actinin-green fluorescent protein. Cell Motil Cytoskeleton 48, 190–200.

Fujiwara K, Porter ME, Pollard TD (1978). Alpha-actinin localization in the cleavage furrow during cytokinesis. J Cell Biol 79, 268–275.

Gallet F, Arcizet D, Bohec P, Richert A (2009). Power spectrum of out-of-equilibrium forces in living cells: amplitude and frequency dependence. Soft Matter 5, 2947–2953.

Gittes F, Mickey B, Nettleton J, Howard J (1993). Flexural rigidity of microtubules and actin filaments measured from thermal fluctuations in shape. J Cell Biol 120, 923–934.

Greenberg MJ, Moore JR (2010). The molecular basis of frictional loads in the in vitro motility assay with applications to the study of the loaded mechanochemistry of molecular motors. Cytoskeleton 67, 273–285.

Guha M, Zhou M, Wang Y-L (2005). Cortical actin turnover during cytokinesis requires myosin II. Curr Biol 15, 732–736.

Hachet O, Simanis V (2008). Mid1p/anillin and the septation initiation network orchestrate contractile ring assembly for cytokinesis. Genes Dev 22, 3205–3216.

Howard J (2001). Mechanics of Motor Proteins and the Cytoskeleton, Sunderland, MA: Sinauer Associates..

Janson LW, Sellers JR, Taylor DL (1992). Actin-binding proteins regulate the work performed by myosin II motors on single actin filaments. Cell Motil Cytoskeleton 22, 274–280.

Kamasaki T, Osumi M, Mabuchi I (2007). Three-dimensional arrangement of F-actin in the contractile ring of fission yeast. J Cell Biol 178, 765–771.

Kim T, Hwang W, Kamm RD (2009). Computational analysis of a cross-linked actin-like network. Experimental Mechanics 49, 91–104.

Klein MG, Shi W, Ramagopal U, Tseng Y, Wirtz D, Kovar DR, Staiger CJ, Almo SC (2004). Structure of the actin crosslinking core of fimbrin. Structure 12, 999–1013.

Kohler S, Schaller V, Bausch AR (2011). Structure formation in active networks. Nat Mater 10, 462–468.

Kojima H, Ishijima A, Yanagida T (1994). Direct measurement of stiffness of single actin filaments with and without tropomyosin by in vitro nanomanipulation. Proc Natl Acad Sci USA 91, 12962–12966.

Kovar DR, Kuhn JR, Tichy AL, Pollard TD (2003). The fission yeast cytokinesis formin Cdc12p is a barbed end actin filament capping protein gated by profilin. J Cell Biol 161, 875–887.

Laporte D, Coffman VC, Lee I-J, Wu J-Q (2011). Assembly and architecture of precursor nodes during fission yeast cytokinesis. J Cell Biol 192, 1005–1021.

Laporte D, Zhao R, Wu J-Q (2010). Mechanisms of contractile-ring assembly in fission yeast and beyond. Semin Cell Dev Biol 21, 892–898.

Lee I-J, Wu J-Q (2012). Characterization of Mid1 domains for targeting and scaffolding in fission yeast cytokinesis. J Cell Sci (*in press*).

Mabuchi I, Hamaguchi Y, Kobayashi T, Hosoya H, Tsukita S (1985). Alpha-actinin from sea urchin eggs: biochemical properties, interaction with actin, and distribution in the cell during fertilization and cleavage. J Cell Biol 100, 375–383.

Maciver SK, Wachsstock DH, Schwarz WH, Pollard TD (1991). The actin filament severing protein actophorin promotes the formation of rigid bundles of actin filaments crosslinked with α-actinin. J Cell Biol 115, 1621–1628.

Martin SG, Chang F (2006). Dynamics of the formin for3p in actin cable assembly. Curr Biol 16, 1161–1170.

Medeiros NA, Burnette DT, Forscher P (2006). Myosin II functions in actin-bundle turnover in neuronal growth cones. Nat Cell Biol 8, 215–226.

Meyer RK, Aebi U (1990). Bundling of actin-filaments by α-actinin depends on its molecular length. J Cell Biol 110, 2013–2024.

Moreno S, Klar A, Nurse P (1991). Molecular genetic analysis of fission yeast Schizosaccharomyces pombe. Methods Enzymol 194, 795–823.

Motegi F, Nakano K, Mabuchi I (2000). Molecular mechanism of myosin-II assembly at the division site in Schizosaccharomyces pombe. J Cell Sci 113, 1813–1825.

Mukhina S, Wang Y-L, Murata-Hori M (2007). α-Actinin is required for tightly regulated remodeling of the actin cortical network during cytokinesis. Dev Cell 13, 554–565.

Murthy K, Wadsworth P (2005). Myosin-II-dependent localization and dynamics of F-actin during cytokinesis. Curr Biol 15, 724–731.

Nakano K, Mabuchi I (2006). Actin-capping protein is involved in controlling organization of actin cytoskeleton together with ADF/cofilin, profilin and F-actin crosslinking proteins in fission yeast. Genes Cells 11, 893–905.

Nakano K, Satoh K, Morimatsu A, Ohnuma M, Mabuchi I (2001). Interactions among a fimbrin, a capping protein, and an actin-depolymerizing factor in organization of the fission yeast actin cytoskeleton. Mol Biol Cell 12, 3515–3526.

Nedelec F, Foethke D (2007). Collective Langevin dynamics of flexible cytoskeletal fibers. New J Phys 9, 427.

Noguchi T, Arai R, Motegi F, Nakano K, Mabuchi I (2001). Contractile ring formation in Xenopus egg and fission yeast. Cell Struct Funct 26, 545–554.

Nolen BJ, Tomasevic N, Russell A, Pierce DW, Jia Z, McCormick CD, Hartman J, Sakowicz R, Pollard TD (2009). Characterization of two classes of small molecule inhibitors of Arp2/3 complex. Nature 460, 1031–1034.

Ojkic N, Vavylonis D (2010). Kinetics of myosin node aggregation into a contractile ring. Phys Rev Lett 105, 048102.

Ojkic N, Wu J-Q, Vavylonis D (2011). Model of myosin node aggregation into a contractile ring: the effect of local alignment. J Phys Condens Matter 23, 374103.

Padmanabhan A, Bakka K, Sevugan M, Naqvi NI, D'Souza V, Tang X, Mishra M, Balasubramanian MK (2011). IQGAP-related Rng2p organizes cortical nodes and ensures position of cell division in fission yeast. Curr Biol 21, 467–472.

Pasquali M, Morse DC (2002). An efficient algorithm for metric correction forces in simulations of linear polymers with constrained bond lengths. J Chem Phys 116, 1834–1838.

Pelham RJ Jr, Chang F (2002). Actin dynamics in the contractile ring during cytokinesis in fission yeast. Nature 419, 82–86.

Pollard TD, Wu J-Q (2010). Understanding cytokinesis: lessons from fission yeast. Nat Rev Mol Cell Biol 11, 149–155.

Reichl EM, Ren Y, Morphew MK, Delannoy M, Effler JC, Girard KD, Divi S, Iglesias PA, Kuo SC, Robinson DN (2008). Interactions between myosin and actin crosslinkers control cytokinesis contractility dynamics and mechanics. Curr Biol 18, 471–480.

Roberts-Galbraith RH, Gould KL (2008). Stepping into the ring: the SIN takes on contractile ring assembly. Genes Dev 22, 3082–3088.

Sanger JM, Mittal B, Pochapin MB, Sanger JW (1987). Stress fiber and cleavage furrow formation in living cells microinjected with fluorescently labeled α-actinin. Cell Motil Cytoskeleton 7, 209–220.

Sato M, Schwarz WH, Pollard TD (1987). Dependence of the mechanical properties of actin α-actinin gels on deformation rate. Nature 325, 828–830.

Schmoller KM, Semmrich C, Bausch AR (2011). Slow down of actin depolymerization by cross-linking molecules. J Struc Biol 173, 350–357.

Scott BJ, Neidt EM, Kovar DR (2011). The functionally distinct fission yeast formins have specific actin-assembly properties. Mol Biol Cell 22, 3826–3839.

Shirayama S, Numata O (2003). Tetrahymena fimbrin localized in the division furrow bundles actin filaments in a calcium-independent manner. J Biochem 134, 591–598.

Sjoblom B, Salmazo A, Djinovic-Carugo K (2008). α-Actinin structure and regulation. Cell Mol Life Sci 65, 2688–2701.

Skau CT, Courson DS, Bestul AJ, Winkelman JD, Rock RS, Sirotkin V, Kovar DR (2011). Actin filament bundling by fimbrin is important for endocytosis, cytokinesis, and polarization in fission yeast. J Biol Chem 286, 26964–26977.

Skau CT, Kovar DR (2010). Fimbrin and tropomyosin competition regulates endocytosis and cytokinesis kinetics in fission yeast. Curr Biol 20, 1415–1422.

Smith MB, Li HS, Shen TA, Huang XL, Yusuf E, Vavylonis D (2010). Segmentation and tracking of cytoskeletal filaments using open active contours. Cytoskeleton 67, 693–705.

Stark BC, Sladewski TE, Pollard LW, Lord M (2010). Tropomyosin and myosin-II cellular levels promote actomyosin ring assembly in fission yeast. Mol Biol Cell 21, 989–1000.

Strehle D, Schnauss J, Heussinger C, Alvarado J, Bathe M, Kas J, Gentry B (2011). Transiently crosslinked F-actin bundles. Eur Biophys J 40, 93–101.

Swartz DR (1999). Exchange of α-actinin in isolated rigor myofibrils. J Muscle Res Cell Motil 20, 457–467.

Vavylonis D, Wu J-Q, Hao S, O'Shaughnessy B, Pollard TD (2008). Assembly mechanism of the contractile ring for cytokinesis by fission yeast. Science 319, 97–100.

Wachtler V, Huang Y, Karagiannis J, Balasubramanian MK (2006). Cell cycle-dependent roles for the FCH-domain protein Cdc15p in formation of the actomyosin ring in Schizosaccharomyces pombe. Mol Biol Cell 17, 3254–3266.

Wachtler V, Rajagopalan S, Balasubramanian MK (2003). Sterol-rich plasma membrane domains in the fission yeast Schizosaccharomyces pombe. J Cell Sci 116, 867–874.

Wang J, Hu H, Wang S, Shi J, Chen S, Wei H, Xu X, Lu L (2009). The important role of actinin-like protein (AcnA) in cytokinesis and apical dominance of hyphal cells in Aspergillus nidulans. Microbiology 155, 2714–2725.

Watanabe S, Ando Y, Yasuda S, Hosoya H, Watanabe N, Ishizaki T, Narumiya S (2008). mDia2 induces the actin scaffold for the contractile ring and stabilizes its position during cytokinesis in NIH 3T3 cells. Mol Biol Cell 19, 2328–2338.

Wu J-Q, Bähler J, Pringle JR (2001). Roles of a fimbrin and an α-actinin-like protein in fission yeast cell polarization and cytokinesis. Mol Biol Cell 12, 1061–1077.

Wu J-Q, Kuhn JR, Kovar DR, Pollard TD (2003). Spatial and temporal pathway for assembly and constriction of the contractile ring in fission yeast cytokinesis. Dev Cell 5, 723–734.

Wu J-Q, McCormick C, Pollard TD (2008). Chapter 9: counting proteins in living cells by quantitative fluorescence microscopy with internal standards. Methods Cell Biol 89, 253–273.

Wu J-Q, Pollard TD (2005). Counting cytokinesis proteins globally and locally in fission yeast. Science 310, 310–314.

Wu J-Q, Sirotkin V, Kovar DR, Lord M, Beltzner CC, Kuhn JR, Pollard TD (2006). Assembly of the cytokinetic contractile ring from a broad band of nodes in fission yeast. J Cell Biol 174, 391–402.

Xu J, Wirtz D, Pollard TD (1998). Dynamic cross-linking by α-actinin determines the mechanical properties of actin filament networks. J Biol Chem 273, 9570–9576.

Ye Y, Lee I-J, Runge KW, Wu J-Q (2012). Roles of putative Rho-GEF Gef2 in division-site positioning and contractile-ring function in fission yeast cytokinesis. Mol Biol Cell 23, 1181–1195.

Zhou M, Wang Y-L (2008). Distinct pathways for the early recruitment of myosin II and actin to the cytokinetic furrow. Mol Biol Cell 19, 318–326.